UNCLASSIFIED

NRL Report 7324

A Neutron Spectrometer Using Organic Scintillators

D. W. JONES AND M. ELAINE TOMS

Linac Branch
Nuclear Sciences Division

PLEASE RETURN THIS COPY TO:

NAVAL RESEARCH LABORATORY
WASHINGTON, D.C. 20375
ATTN: CODE 2628

Because of our limited supply you are requested to return this copy as soon as it has served your purposes so that it may be made available to others for reference use. Your cooperation will be appreciated.

NDW-NRL-5070/2651 (Rev. 9-75)

LOAN COPY

November 10, 1971

NAVAL RESEARCH LABORATORY
Washington, D.C.

Approved for public release; distribution unlimited.

UNCLASSIFIED

CONTENTS

Abstract iii
Problem Status iii
Authorization iii
Table of Symbols iv

INTRODUCTION 1

1. GENERAL DESCRIPTION OF NEUTRON SPECTROMETER 2

   1.1 Block Diagram of Neutron Spectrometer 2
   1.2 Scintillation Counter 3
   1.3 Pulse Amplifiers and Pulse-Height Analyzer 5
   1.4 Summary and Comment 6

2. PULSE-HEIGHT DATA FROM RECOIL PROTONS 7

   2.1 Introduction 7
   2.2 Neutron-Proton Elastic Scattering 7
   2.3 Nonlinear Pulse-Height Response 8
   2.4 Perturbations of the Ideal Recoil-Proton Spectrum 12
      (a) Second Scattering of Neutrons 12
      (b) Loss of Recoil Protons 13
      (c) Elastic Scattering from Carbon 15
      (d) Inelastic Scattering from Carbon 16
      (e) Alpha-Producing Reactions 17
   2.5 Interpretation of Perturbations 18

3. DATA ANALYSIS AND COMPUTER CODE 19

   3.1 Data Analysis 19
   3.2 Computer Code 22
   3.3 Programming for a Small Computer 23

4. EXAMPLES OF DATA ANALYSIS 24

   4.1 Monoenergetic Neutron Spectra 24
   4.2 Energy Spectra for Neutrons from α-n Sources 27
   4.3 Other Spectra 29
   4.4 Uranium Assay 30

5. PULSE-SHAPE-DISCRIMINATION CIRCUIT 32

5.1 General Description 32
5.2 Pulse-Shape Discrimination 35
5.3 Logic Circuits 39
5.4 Summary and Comment 41

REFERENCES 43

APPENDIXES

APPENDIX 1—Energy Distributions of Reaction Products 45
APPENDIX 2—Summary of Energy Calibrations for Stilbene 50
APPENDIX 3—Derivation for Second Scattering by Hydrogen 51
APPENDIX 4—Derivation of Effects due to Loss of Protons 53
APPENDIX 5—Table of Response Function and Cross Sections 56
APPENDIX 6—Table of Efficiencies and ψ-Functions 58
APPENDIX 7—Listing of Computer Code in FORTRAN 62
APPENDIX 8—Computer Output Table for *PuBe*-Neutron Data 64
APPENDIX 9—Computer Output Table for 8-MeV Neutrons 66

UNCLASSIFIED

ABSTRACT

Organic scintillation detectors are useful for neutron spectroscopy because pulses induced by gamma rays and those induced by neutrons can be distinguished by electronic means. Computer analysis can be used to obtain the energy spectrum of the neutrons from the measured recoil-proton pulse-height distribution. This report describes a practical neutron spectrometer with improved electronic circuitry for pulse-shape discrimination. A detailed study of the interaction of neutrons with the scintillator is presented in relation to pulse-height analysis. A computer program that uses a straightforward method of pulse-height analysis is given in FORTRAN with suggestions for adaptation for use on a small computer. Spectrometer applications are presented for measuring neutron spectra of monoenergetic neutrons, radioactive neutron sources, scattered neutrons and neutrons from a photonuclear reaction and also for detection of fission neutrons.

PROBLEM STATUS

This is a final report on this neutron spectrometer.

AUTHORIZATION

NRL Problem H01-09
Project RR 002-06-41-5005

Manuscript submitted July 8, 1971.

TABLE OF SYMBOLS

N_o	Flux of incident neutrons (neutrons/unit area)
E_o	Energy of incident neutrons (MeV)
A	Area of the detector (cm^2)
L	Length of the detector (generally cm)
N_p	Total number of recoil protons produced in the detector
E	Energy of protons or neutrons (MeV)
$\epsilon(E,L)$	Efficiency of the detector for producing recoil protons (c.f. Sec. 2.2)
n_h	Protons per unit volume of the detector
n_c	Carbon atoms per unit volume of the detector
$\sigma_h(E)$	Neutron-proton scattering cross section
$\sigma_c(E)$	Total neutron interaction cross section with carbon
a	Reciprocal of the absorption length, $a = n_h\sigma_h(E) + n_c\sigma_c(E)$
N	Flux of neutrons within the detector, $N = N_o e^{-ax}$
dE/dx	Rate of energy loss by charged particles in the detector
$R(E)$	Range of proton of energy E in the detector
P	Electron energy (MeV)
dN_p/dE	Recoil-proton flux per unit energy
dN_p/dP	Recoil-proton flux per unit electron energy
dN_n/dE	Neutron flux per unit energy
$N_p(E)$	Total recoil protons per unit energy ($A\ dN_p/dE$)
$N_p(P)$	Total recoil protons per unit electron energy ($A\ dN_p/dP$)
$N_n(E)$	Total neutrons per unit energy ($A\ dN_p/dP$)
PSD	Pulse shape discrimination

UNCLASSIFIED

A NEUTRON SPECTROMETER USING ORGANIC SCINTILLATORS

D.W. Jones* and M.E. Toms

INTRODUCTION

In the past decade interest has increased in the use of organic scintillation detectors for neutron spectroscopy. Historically these scintillators were of little more than academic interest because of the difficulty involved in analyzing pulse-height spectra obtained from these detectors and because of their inherent sensitivity to gamma rays. More recently, methods have been developed to distinguish the pulses which are induced by neutrons from those induced by gamma rays, and to derive the energy spectrum of the neutrons incident upon the detector from the measured pulse-height distribution. The recent interest is due in part to these developments and in part to the availability of small computers which are needed for data analysis.

The object of an extensive program at NRL during the years from 1966 to 1969 has been to develop a practical neutron spectrometer using organic scintillators. The spectrometer developed at NRL consists of (a) a scintillation counter with an organic crystal as the fast-neutron detector, (b) a circuit for analyzing the shape of the current pulse from the scintillation counter to identify the particle which induced the scintillation, (c) a pulse-height analyzer and associated electronics for collecting the pulse-height data and (d) a computer program for analyzing the pulse-height data to extract the energy spectrum of the neutrons incident upon the face of the detector.

In the development of this spectrometer the optimum electronic system necessary for collecting data was studied in detail, and a new electronic circuit for analyzing the shape of the current pulse from the scintillation counter was developed. The interaction of neutrons with the scintillator was also studied in detail to obtain a nearly optimum method of pulse-height analysis. The neutron spectrometer developed at NRL has been used to measure both monoenergetic neutron spectra and continuous neutron spectra. In this report, a detailed explanation will be given of the electronic systems of the spectrometer and the analysis of the experimental pulse-height data to obtain the energy spectrum of the neutrons incident upon the detector. Examples will also be presented of the application of this spectrometer to the measurement of both continuous and discrete neutron energy spectra.

The primary purpose of this development was to provide a neutron spectrometer for photonuclear spectroscopy. During the course of this development the spectrometer has been applied to (a) measurement of the energy spectrum of monoenergetic neutrons produced by $D(d,n)$, $T(p,n)$, and $T(d,n)$ reactions; (b) measurement of the energy spectra of neutrons from the radioactive α-beryllium sources: *PuBe*, *AmBe*, and *PoBe*; (c) measurement of neutron elastic and inelastic cross sections; (d) measurement of the energy spectrum

*Present address: Memphis State University, Memphis, Tennessee.

of neutrons from the photonuclear reaction produced by 28-MeV bremsstrahlung on oxygen-16; and (e) detection of fission neutrons from uranium and plutonium isotopes for a Safeguards application. Most of these applications will be discussed in this report. Other potential fields of use include health physics, nuclear bomb tests, and any other need involving the measurement of fast neutrons.

The authors of this report acknowledge the use of the NRL Van de Graaff facilities for taking data and the advice of Dr. P. Malmberg and Dr. T. May. The advice of Dr. W.L. Bendel in the early stages of the computer programming is appreciated. Also the encouragement and advice of Dr. T.F. Godlove throughout the course of the development of this spectrometer are appreciated.

1. GENERAL DESCRIPTION OF NEUTRON SPECTROMETER

1.1 Block Diagram of Neutron Spectrometer

A block diagram of the neutron spectrometer developed at NRL is shown in Fig. 1.1. The scintillation counter consists of an organic scintillation detector, either stilbene or NE 213, mounted on a photomultiplier capable of high current output. Two pulses are taken from the photomultiplier: one from the anode and one from the 11th dynode. The pulse from the 11th dynode is integrated in a preamplifier to obtain an output voltage with an amplitude proportional to the total charge contributed by the scintillation to the charge pulse in the multiplier. This pulse is then shaped and increased by a linear amplifier to obtain a voltage pulse with an amplitude and shape compatible with the input to a 1024-channel pulse-height analyzer.

Because the detector is sensitive to both neutrons and gamma rays, it was necessary to develop a pulse-shape discrimination (PSD) circuit which analyzes the shape of the current pulse from the photomultiplier anode to determine the identity of the particle which induced the scintillation in the detector. The current pulse from the photomultiplier develops a voltage pulse at the input to this circuit across the terminating resistor of a length of coaxial

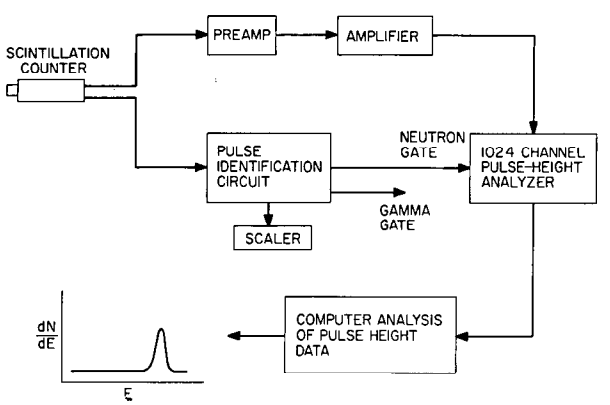

Fig. 1.1—Block diagram of neutron spectrometer

UNCLASSIFIED

cable. For the electronic analysis of the scintillation pulse the shape of the current pulse must be preserved at the input to this circuit; this purpose is achieved by properly terminating the 100-foot-long coaxial cables normally used in this spectrometer. If the PSD circuit determines that the scintillation in the detector was induced by a neutron, it provides a logic pulse to open the coincidence gate of the pulse-height analyzer. Therefore, only those pulses which were induced in the detector by neutrons are admitted to the pulse-height analyzer. A gamma gate is also provided by the PSD circuit if pulses induced in the detector are identified as due to gamma rays. This gating pulse may be used in a similar manner to simultaneously collect the pulse-height distribution due to gamma rays in another pulse-height analyzer. A third pulse permits the total number of pulses to be counted in a scaler or the counting rate to be measured in a count rate meter.

Because of the nature of the detector response, the pulse-height distribution stored in the analyzer does not bear a simple relationship to the energy spectrum of the neutrons incident upon the face of the detector. It was necessary, therefore, to develop a computer program to analyze the pulse-height distribution. The computer program developed at NRL derives the energy spectrum of the incident neutrons by first converting the pulse-height data to the energy spectrum of recoil protons and then calculating the neutron energy spectrum by differentiating the recoil proton spectrum. In Chapter 2 is a discussion of pulse-height data from recoil protons described in terms of an ideal proton spectrum with perturbations. Data analysis and the FORTRAN computer program are given in Chapter 3.

In the following sections, the details related to the construction of the scintillation counter will be discussed. Since the equipment used to collect the pulse-height data is commercially available, only those principles important to the selection of this equipment will be outlined. The details of the PSD circuit developed at NRL will be given in Chapter 5.

1.2 Scintillation Counter

A cross-sectional diagram of the scintillation counter is shown in Fig. 1.2. As indicated by this diagram, the scintillation counter consists of (a) a scintillation crystal, (b) a photomultiplier with electrostatic and magnetic shielding, (c) a high-voltage divider and the base for the photomultiplier tube, and (d) an aluminum case. An RCA-6810A photomultiplier was selected because the photocathode has high quantum efficiency and its response matches the emission spectrum from organic scintillators. This tube is capable of a high current output, thus eliminating the need for an amplifier preceding the PSD circuit. The cathode is operated at negative potential (nominally at 2000 V), and the anode is at ground potential to permit a signal to be taken directly from the anode without the need for a large coupling capacitor. A charge pulse is taken from the 11th dynode to provide a linear signal to the preamplifier.

To insure linearity over a large signal range the voltage divider, shown in Fig. 1.3 is used. This divider distributes a larger fraction of the anode-cathode voltage over the last few dynodes than dividers designed for high gain service. For proper operation of the PSD circuit it is necessary that both the total charge output of the photomultiplier be proportional to the total light output of the scintillator and the peak current output from the photomultiplier be proportional to the peak light output of the scintillator. The linearity of this

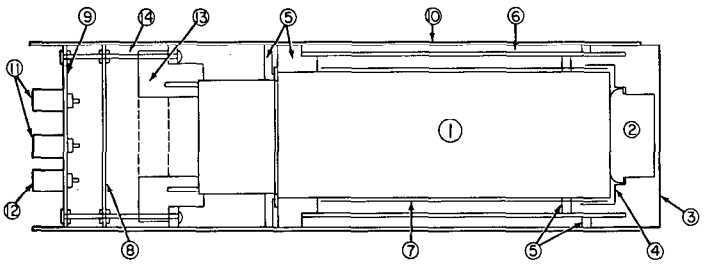

Fig. 1.2—Cross section of scintillation counter assembly:
1. RCA 6810A photomultiplier
2. Stilbene detector
3. Front-end cap (0.020-in. Al)
4. Holder for detector (0.020-in. Al)
5. Teflon spacers
6. Magnetic shield
7. Electrostatic shield
8. Divider string for PM
9. Back-end plate (0.060-in. Al)
10. Outside case (0.060-in. Al)
11. Output connectors
12. High-voltage input
13. PM base socket
14. Spacing screws.

peak current, up to 300 mA, is insured by having each dynode bypassed to ground through a capacitor large enough to reduce the signal voltage at that dynode to less than 1% of the voltage between that dynode and the adjacent ones. With this divider the current output of the photomultiplier is proportional to the light output of the scintillator up to a peak output current of 0.5 A.

Because of the negative potential applied to the cathode, both the electrostatic and magnetic shields must be maintained at high voltage. Insulation from the outside case is provided by Teflon spacers. The entire assembly is contained within a thin-walled aluminum tube with light-tight end caps. To reduce the neutron interactions with the scintillation-counter hardware, the thickness of the front end cap was reduced to 0.020 inch and the wall thickness of the tube to 0.060 inch.

The gain of the photomultiplier is largely dependent upon the voltage impressed between the anode and the cathode of the photomultiplier with the fractional gain dG/G approximately equal to $N\,dV/V$, where $N \approx 10$ for a 14-stage tube. As will be pointed out in Chapter 4, an overall system stability of ±1% is required when it is desired to define the energy of the neutrons incident upon the detector to within 0.1 MeV. Power supplies stable to within ±0.01% over the range of operating conditions are normally selected for this purpose.

UNCLASSIFIED

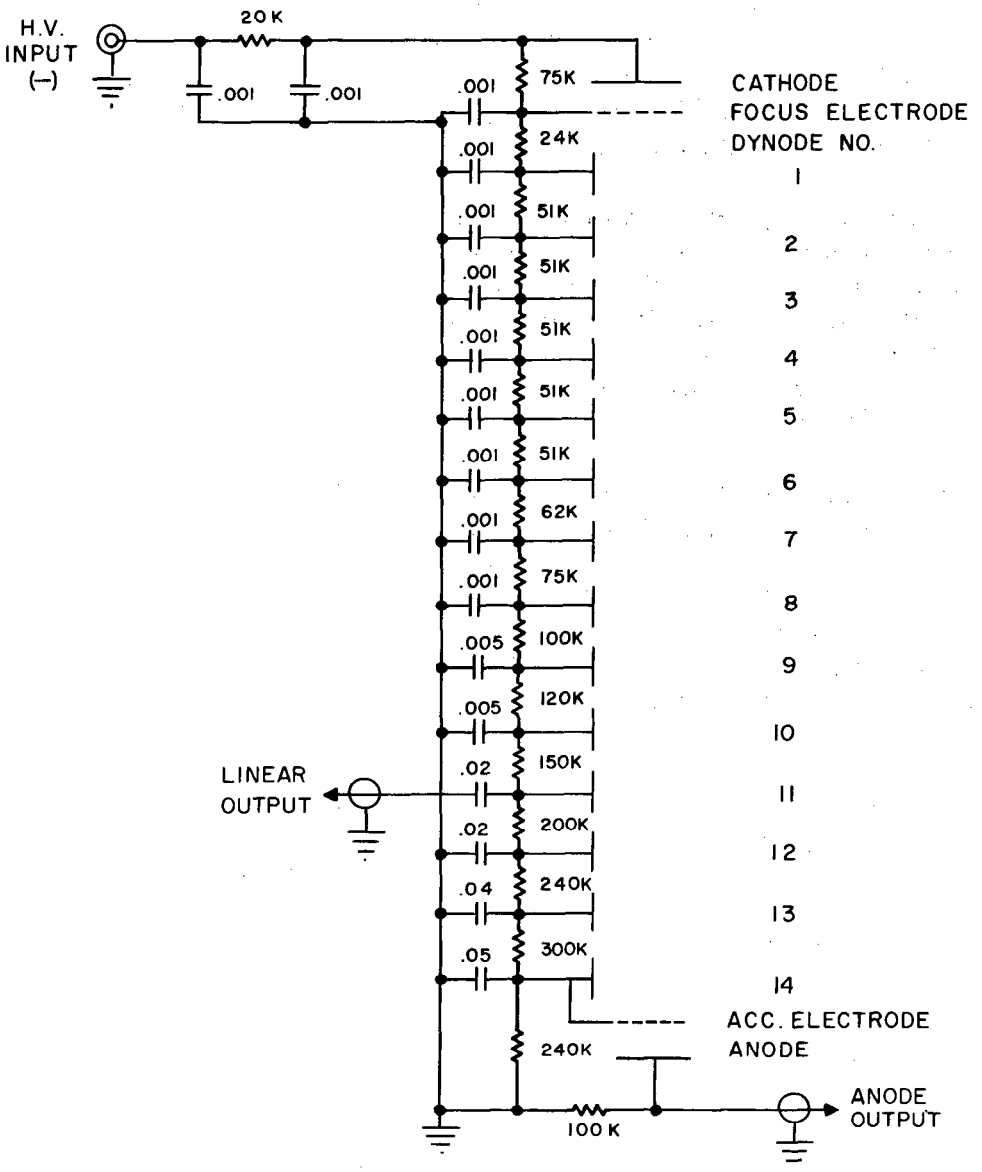

Fig. 1.3—High-voltage divider string for RCA 6810A. All resistors are rated at 1/2 watt and 5%. All capacitors are listed in microfarads. The ratings for the capacitors are: 3 kV for 0.001 μF; 2 kV for 0.005 μF and 0.02 μF; and 1 kV for 0.04 μF and 0.05 μF.

1.3 Pulse Amplifiers and Pulse-Height Analyzer

As illustrated in Fig. 1.1, the system used to collect a pulse-height distribution from the scintillation counter consists of (a) a preamplifier for integrating the charge pulse from the photomultiplier to obtain a voltage pulse proportional to the total charge pulse, (b) a linear amplifier for shaping and amplifying the voltage pulse to a range compatible with the input to the pulse-height analyzer, and (c) a pulse-height analyzer to collect the pulse-height data.

The output of the integrating preamplifier is determined by the magnitude of the charge delivered from the photomultiplier and is independent of the pulse shape only if the integrating time constant of the preamplifier is much larger than the decay time of the pulse from the photomultiplier. If the decay of the scintillation pulse is approximated by a series of exponentials, the decay time of the longest large component is about 300 nsec. Therefore, the integrating time constant of the preamplifier should exceed 10 μsec.

Both charge-sensitive preamplifiers and RC-integrating networks with emitter followers have been used successfully in this spectrometer. Either type is normally located near the photomultiplier, and its output is driven through a long cable to a remote linear amplifier. Because of electromagnetic pickup, it is often necessary to operate both amplifiers remotely from the scintillation counter. In this case, the current pulse from the scintillation counter may be converted to a voltage pulse developed across a cable termination and then integrated in an operational amplifier.

The primary purpose of the linear amplifier is to shape the preamplifier output so that a high counting rate may be obtained. For this purpose a double-delay-line amplifier is used in this spectrometer. The voltage gain serves only to convert the amplitude of the output from the preamplifier to a level compatible with the input of the pulse-height analyzer, while the double-delay-line differentiation reduces the effective width of the pulse to about 2 μsec. Although a shorter clipping time constant would permit higher counting rates, less than 2 μsec should not be used since the integrated charge pulse due to recoil protons does not reach its final amplitude until about 2 μsec after its appearance.

As will be discussed in Chapter 2, the sensitivity of the detector to both neutrons and gamma rays provides a unique method of calibrating the energy response of the detector. It is found that this calibration depends upon the characteristics of the detector rather than the electronics only if the current pulse of the scintillator is integrated with a time constant greater than 10 μsec and the clipping time constant of the linear amplifier is set to no less than 2 μsec.

The PSD circuit requires 1 μsec to analyze the current pulse from the photomultiplier to identify the particle which induced the pulse. Therefore, a delay of 1 μsec is required between the linear amplifier and the pulse-height analyzer. Often this delay may be obtained from the delayed output of a linear amplifier. The length of the delay varies with the type of pulse-height analyzer used.

1.4. Summary and Comment

In this chapter the basic features of the NRL neutron spectrometer have been described. The spectrometer is designed such that the scintillation counter can be operated remotely from the PSD circuit and the electronics used to collect pulse-height data. The upper limit of the energy range of the spectrometer is limited by the linearity of the photomultiplier while the lower limit of the energy range is established by the neutron-gamma discrimination ratio of the PSD circuit. Within these limits an operating range of 2 to 15 MeV neutron energy has been achieved. Within this range, the resolution of the spectrometer varies from 12.5% at 4.0 MeV to 6.5% at 8 MeV. The overall resolution of the spectrometer is limited

UNCLASSIFIED

primarily by the light conversion efficiency of the photocathode of the photomultiplier. Examples of measurements which exhibit this resolution are given in Chapter 4.

2. PULSE-HEIGHT DATA FROM RECOIL PROTONS

2.1. Introduction

Although neutrons interact with the hydrogen and carbon nuclei of organic scintillators by several different mechanisms, the detection of neutrons by an organic scintillator depends primarily upon elastic scattering collisions between neutrons and protons. From the scattering collisions a continuous distribution of recoil protons is obtained. These protons range in energy from zero up to the energy of the neutrons which produced them. As will be explained in this chapter, the energy-response function of the scintillator is nonlinear; therefore, the pulse-height distribution obtained from the scintillation counter will not be directly proportional to the energy spectrum of the recoiling protons. When the response function is determined, the pulse-height distribution can be converted to the recoil-proton energy spectrum, and a differentiation process can then yield the energy spectrum of the incident neutrons. This method is applicable both when the incident-neutron energy spectrum is monoenergetic and when it is continuous.

Other reactions of neutrons with the atoms of the detector serve to produce scintillations which may be considered as perturbations to the recoil-proton energy spectrum. Some of these reactions are (a) second scattering of the neutrons from hydrogen nuclei; (b) loss of recoiling protons through the end of the detector; and (c) elastic scattering, inelastic scattering, and other reactions with carbon atoms of the detector. The effect of each of these perturbations will be discussed in this chapter.

Gamma rays interact with the scintillator primarily by the Compton scattering process. As a result of these scattering collisions, recoiling electrons are produced which range in energy from zero up to a maximum energy called the Compton edge. The response of the scintillator to these recoil electrons is linear. This linear response provides a method by which the energy scale of the pulse-height analyzer can be calibrated before each experiment with gamma-ray sources provided that the electron and proton energies for equal response are known. This relation between the electron and proton energies for equal response and the method of calibration will be discussed in detail in this chapter.

2.2. Neutron-Proton Elastic Scattering

If we consider a beam of neutrons of energy E_o with a flux N_o incident upon a hydrogenous scintillator of area A and length L, it follows that the total number of protons N_p produced by single scattering collisions is given by

$$N_p = N_o A \epsilon(E_o, L), \tag{2-1}$$

where $\epsilon(E_o,L)$, the efficiency of the scintillator for producing recoil protons by single scattering collisions, is given (1) by

$$\epsilon(E_o,L) = n_h\sigma_h L(1 - e^{-aL})/aL = n_h\sigma_h L f(aL),$$

with (2-2)

$$a = n_h\sigma_h + n_c\sigma_c \text{ and } f(aL) = (1 - e^{-aL})/aL.$$

In this formula, n_h and n_c refer, respectively, to the numbers of hydrogen and carbon atoms per unit volume of the scintillator, σ_h is the neutron-proton scattering cross section, and σ_c is the total carbon interaction cross section for neutrons. This formula for the single-scattering efficiency neglects the possible production of recoil protons by neutrons once scattered by hydrogen or carbon.

As pointed out by Staub (2), it can be shown kinematically that the number of recoiling protons per unit energy in the laboratory system is proportional to the differential elastic-scattering cross section per unit solid angle in the center-of-mass (c.m.) system. If the neutron-proton scattering is considered to be isotropic in the c.m. system, the recoil proton distribution in the scintillator is given by the following formula which is derived in Appendix 1 (c.f. Eq. (A1-28)), for a monoenergetic incident beam:

$$N_p(E) = A\, dN_p/dE = [N_o A\epsilon(E_o,L)]/E_o. \tag{2-3}$$

If the spectrum of the incident neutrons is not monoenergetic but has a distribution dN_n/dE_o (neutrons per unit area per energy interval), then we must include the contribution to $N_p(E)$ of all neutrons above the energy E. Thus, in general

$$N_p(E) = \int_E^\infty [A\epsilon(E_o,L)/E_o](dN_n/dE_o)\, dE_o. \tag{2-4}$$

Differentiating both sides with respect to E and solving gives the energy spectrum of the incident neutrons in terms of the slope of the recoil-proton energy spectrum:

$$(dN_n/dE_o)_E = dN_n/dE = -(dN_p(E)/dE)[E/(A\epsilon(E,L))]. \tag{2-5}$$

Thus, from the energy of the recoiling protons, the energy spectrum of the incident neutrons can be obtained. However, an organic scintillator produces a pulse-height distribution which is nonlinear with respect to recoil-proton energies, and its output is subject to a number of perturbations which will be discussed.

2.3. Nonlinear Pulse-Height Response

Within the linear range of the photomultiplier, the total charge output of the scintillation counter is proportional to the total luminous output of the scintillation crystal. Details of the scintillator response have been outlined by Schwartz and Owen (1) and by Birks (3). As these authors point out, the luminous output of the scintillation crystal is, in general, not

UNCLASSIFIED

proportional to the energy lost in the scintillator by the charged particle. To describe this nonlinear response, the light output per unit energy loss in the crystal dS/dE can be related to the rate of energy loss by the charged particle dE/dx as it passes through the crystal (1) by

$$dS/dE = C[1 + kB(dE/dx)]^{-1}. \tag{2-6}$$

In this formula, the product of B, a constant, and dE/dx gives the specific density of ionized and excited molecules along the particle track. The quenching parameter k is characteristic of the scintillator for the particular ionizing particle, and C is a proportionality constant.

As Schwartz and Owen (1) observed, there are two limiting forms of Eq. (2-6). For light particles, such as electrons, dE/dx is small enough that the factor $kB(dE/dx)$ can be neglected and the integrated light output due to electrons S_e is proportional to their energy loss in the scintillator:

$$S_e = CE_e. \tag{2-7}$$

For heavier particles, such as protons, alpha particles, and ionized atoms, the factor $kB(dE/dx)$ cannot be neglected; hence, S is not directly proportional to the energy loss of the particle in the scintillator. For very heavy particles, such as fission fragments, dE/dx is sufficiently large that the term $kB(dE/dx)$ dominates the denominator of Eq. (2-6). When this occurs, the integrated light output S_p becomes proportional to the range $R(E)$ of the particle in the scintillator:

$$S_p = CR(E)/kB. \tag{2-8}$$

As a result of this nonlinearity, the pulse-height distribution collected in the pulse-height analyzer will not be proportional to the recoil-proton energy spectrum expressed as $N_p(E)$ in Eqs. (2-3) and (2-4). However, the pulse-height distribution can be converted to a recoil-proton energy spectrum if the response of the scintillator is known.

A convenient method of expressing the response of the scintillator is suggested by the linear relationship between the light output and the electron energy (c.f. Eq. (2-7)). The response can be expressed in terms of the electron and proton energies for equal total light output of the scintillator. When this is done, only an electron energy calibration of the pulse-height analyzer is needed to convert the pulse-height distribution to the recoil-proton energy spectrum. This electron energy calibration can be obtained from the Compton electrons produced in the scintillator by gamma rays as will be explained in this section. Thus, the need for a difficult proton energy calibration prior to each experiment is eliminated.

Some early data giving electron and proton response characteristics for several scintillators are summarized by Birks (3). The relation between the electron and proton energies for equal light output can probably be expressed best by a polynomial. However, the results of several experiments, listed in Appendix 2, demonstrate that the formula below can be used over the range from 2 to 15 MeV as a good approximation of the relation between the electron energy P and the proton energy E for equal light output.

$$P = \alpha E^{\beta}. \tag{2-9}$$

The constants α and β must be determined for each spectrometer; they depend primarily upon the type of scintillator used and its characteristics rather than the electronic system, provided that care is taken to insure that the pulse-height distribution collected in the pulse-height analyzer is proportional to the total light output of the scintillator (c.f. Section 1.3).

An example of the distortion produced by this nonlinear response is shown in Fig. 2.1, where the recoil-proton energy spectrum ($A\ dN_p/dE = N_p(E)$) was calculated from Eq. (2-3) and the recoil-proton pulse-height distribution ($A\ dN_p/dP = N_p(P)$) was calculated from Eq. (2-9). In this figure the recoil-proton pulse-height distribution is expressed in terms of the electron energy for equal charge response. The calculation was performed for monoenergetic neutrons of 8.0 MeV incident upon a stilbene scintillator 1 inch in diameter and 1 inch long. The constants α and β used are 0.150 and 1.5414 respectively with P and E expressed in MeV. As may be seen from this figure, the recoil-proton pulse-height distribution is distorted toward the lower energies and must be converted to a recoil-proton energy spectrum before a differentiation can yield the incident neutron spectrum.

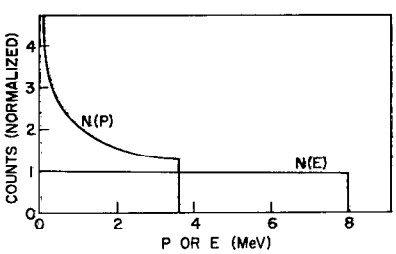

Fig. 2.1—Recoil-proton energy spectrum $N_p(E)$, here denoted as $N(E)$, produced by 8.0-MeV neutrons incident upon a stilbene crystal. The recoil-proton pulse-height distribution $N_p(P)$, here denoted as $N(P)$, is calculated from Eq. (2-9).

To obtain the response-function constants α and β of Eq. (2-9) for the neutron spectrometer discussed in Chapter 1, the electron and proton energies for equal charge response were measured in the following way. For the proton energy calibration, monoenergetic neutrons were obtained from $D(d,n)He^3$ and $T(p,n)He^3$ reactions using the facilities of the NRL 5-MV Van de Graaff. As an example, the pulse-height data obtained from monoenergetic 8.0-MeV neutrons are shown in Fig. 2.2. This distribution resembles the calculated distribution $N_p(P)$ shown in Fig. 2.1. For each of the pulse-height distributions needed for the proton energy calibration, the midpoint on the dropoff was used to determine the channel number corresponding to the maximum recoil-proton energy which equals the energy of the incident neutrons. The electron energy calibration of the pulse-height analyzer was obtained using monoenergetic gamma-ray sources. Gamma rays interact with the detector primarily by Compton scattering collisions with atomic electrons of the detector. The maximum energy of the recoiling electrons E_c commonly referred to as the Compton edge, bears a simple relationship to the energy of the gamma rays E_γ

$$E_c = E_\gamma/(1 + m_0c^2/2E_\gamma). \tag{2-10}$$

As an example, the pulse-height spectrum obtained from a monoenergetic source of gamma rays is shown in Fig. 2.3. The energy scale of the pulse-height analyzer is calibrated by assigning the energy of the Compton end point to the channel corresponding to the midpoint

UNCLASSIFIED

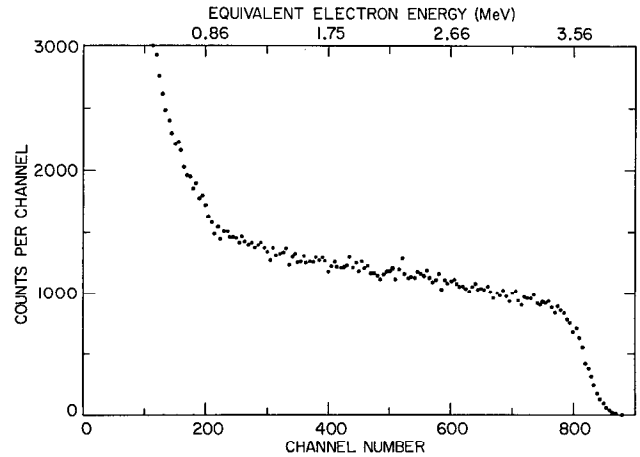

Fig. 2.2—Measured recoil-proton pulse-height distribution produced by 8.0-MeV neutrons incident upon a 1-inch-diameter-by-1-inch long stilbene crystal.

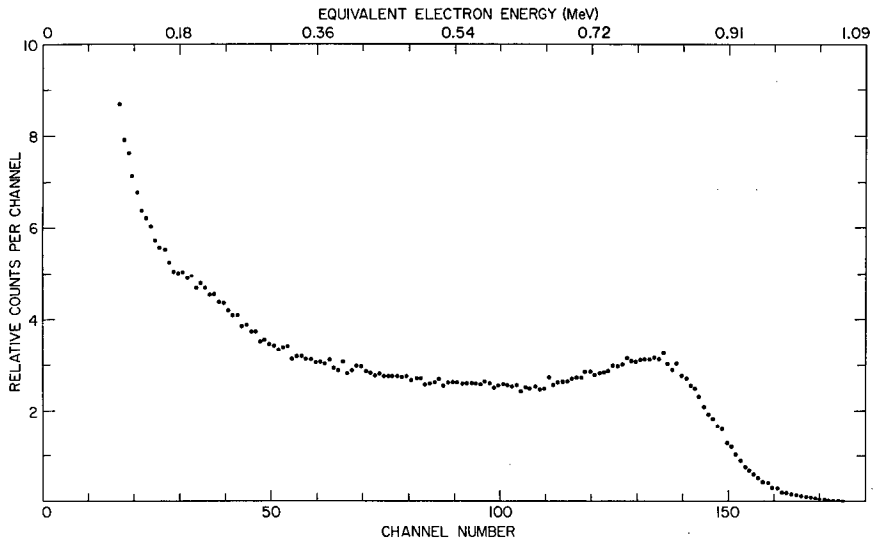

Fig. 2.3—Pulse-height spectrum produced by recoiling Compton electrons produced by monoenergetic gamma rays from Zn^{65}.

of the dropoff in the Compton spectrum. By comparing the electron energy calibration obtained using a number of gamma-ray sources with the proton energy calibration, the electron and proton energies for equal charge response are determined. The results of this measurement are shown in Fig. 2.4. From a straight line fitted to these data points, the constants α and β were found to be 0.150 and 1.5414, respectively. The response curves determined by Wasson (4) for alpha particles and recoiling C^{12} nuclei are also shown on this graph. Calibrations obtained by various experimenters are given in Appendix 2. The variation in slope and intercept of these calibrations is likely due to differences in values of the clipping time constants described in Section 1.3.

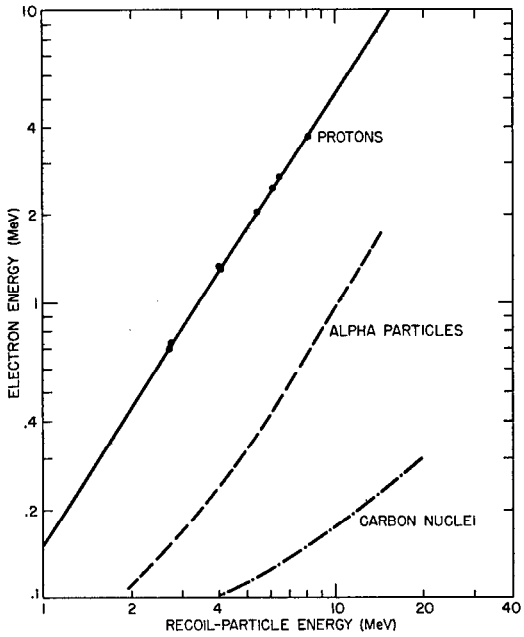

Fig. 2.4—Recoil-particle energy vs electron energy for equal charge response of a stilbene scintillation spectrometer. The points represent NRL data; the curves for alpha particles and carbon nuclei are from Ref. 4.

2.4. Perturbations of the Ideal Recoil-Proton Spectrum

In addition to the nonlinear response of the detector described in the preceding section, several perturbations to the detector response are introduced by the finite size of the detector, second scattering of neutrons by hydrogen, and elastic or inelastic scattering by carbon prior to scattering by hydrogen. These perturbations have been discussed by Schwartz and Owen (1) and by Broek and Anderson (5) for stilbene scintillators and by Batchelor et al. (6) for NE 213 detectors. The effect of these perturbations may be considered as producing distortions to the recoil-proton energy spectrum $N_p(E)$. These effects are discussed below and will be illustrated as distortions of a recoil-proton spectrum produced by a beam of monoenergetic neutrons of 8.0 MeV in a crystal 1 inch long and 1 inch in diameter.

2.4(a) Second Scattering of Neutrons

Because the efficiency for neutron-proton scattering increases with decreasing neutron energy, there is a high probability that a neutron, once scattered from a hydrogen nucleus, will collide with a second proton before escaping from the crystal. Consideration of the velocity of the neutron (1.5 nsec/cm for a 1-MeV neutron), along with the dimensions of commonly used scintillators, indicates that the pulses due to both protons will be separated by little more than a nanosecond. Since the decay time of the scintillation pulse is several nanoseconds, the light from both pulses will add and only one pulse will appear at the output of the photomultiplier. Therefore, the effect of a second scattering event is to remove a proton from the ideal recoil-proton energy spectrum $N_p(E)$ given by Eq. (2-3) and replace it by one whose energy is the sum of the one removed and the energy of the proton recoiling from the second collision. The neutron recoiling from the first collision in which a proton of energy E is produced has an energy $E_o - E$. Protons scattered by collisions with these

UNCLASSIFIED

neutrons will have an energy distribution ranging from zero up to $E_o - E$; therefore, the energy of the sum pulse will range from E to E_o. This summation in effect removes protons from the recoil spectrum at E and redistributes them from E to E_o. For simplicity, the proton energies are assumed to add although the scintillation response is nonlinear.

As shown in Appendix 1, the energy distribution of neutrons scattered from hydrogen dN_n/dE is identical in magnitude and shape to the recoil-proton energy distribution dN_p/dE. Therefore, the number of neutrons of energy $E_o - E$ which participate in a second scattering event is given by $N_p(E)\epsilon(E_o - E,L')$, where $\epsilon(E_o - E,L')$ is the efficiency of the detector for neutron-proton scattering for neutrons of energy $E_o - E$ produced inside the detector. The ideal recoil-proton energy spectrum $N_p(E)$ distorted by the second scattering of incident neutrons may be described as

$$N'_p(E) = N_p(E) - N_p(E)\epsilon(E_o - E,L') + \int_0^E [N_n(E)\epsilon(E_o - E,L')/(E_o - E)]\, d(E_o - E). \tag{2-11}$$

In this formula $N'_p(E)$ represents the distorted spectrum, and the second term represents those recoil protons removed from $N_p(E)$ at E per energy interval. The third term represents the number of protons added to the distribution at E after removal from the lower energy range by a second scattering event as explained above. This term is based on the assumption that the scintillation outputs due to the two protons add linearly. If it is assumed that the efficiency of the scintillator can be approximated by a function of the form KE^{-m} where $K = K(L')$ and $m \approx 0.5$, it is possible to perform the integration and thus derive from Eq. (2-11) an expression given by Schwartz, Owen, and Ames (7) (c.f. Appendix 3):

$$N'_p(E) = N_p(E) \left\{1 + K[(m^{-1} - 1)(E_o - E)^{-m} - m^{-1}E_o{}^{-m}]\right\}. \tag{2-12}$$

Using Eq. (2-11), the distorted recoil spectrum $N'_p(E)$ of protons resulting from 8.0-MeV neutrons has been calculated and is shown in Fig. 2.7a. As can be observed from this diagram, the effect of second scattering is to remove protons from the lower energy range and redistribute them in the upper energy range.

2.4(b) Loss of Recoil Protons

The range of a recoiling proton varies from approximately 0.02 mm at 1 MeV to 1 mm at 10 MeV. Therefore, a fraction of the recoil protons will escape the detector before losing all their energy. To calculate the effect of the loss of these protons from the crystal upon the ideal recoil-proton energy spectrum $N_p(E)$, we consider the protons lost through the end of the crystal and the protons lost through the sides separately. The geometry for the loss of protons through the end of the crystal is given in Fig. 2.5. The number of protons produced in the slab of thickness dx at a distance Z from the end of the crystal is given by $N_oAe^{-ax}n_h\sigma_h\, dx$, and their energy is determined by the angle of recoil $E = E_o \cos^2\theta$. The recoiling proton loses all its energy in the crystal only if the range traversed r is equal to the range $R(E)$ of the proton in the crystal. Therefore, the minimum distance Z_1 from the back surface at which a proton of energy E may be produced and still lose all its energy is given by $Z_1 = R(E)\cos\theta = R(E)(E/E_o)^{1/2}$.

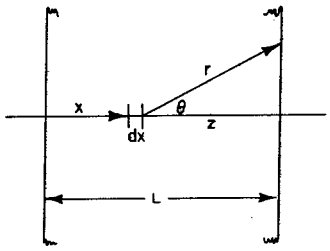

Fig. 2.5—Diagram for deriving the effect of proton loss through the end of a scintillator.

Protons of energy E produced in the region $Z < Z_1$ will never lose all their energy in the crystal and, therefore, will contribute to the recoil-proton energy spectrum at a lower energy. In the same way the numbers of protons at E may have contributions from protons produced in the crystal with energies greater than E. These protons will be produced in the region $Z_1 \leqslant Z \leqslant Z_2$, where Z_2 is the distance from the end of the crystal which will allow a proton of energy E_o recoiling in the forward direction to lose an amount of energy E in the crystal. The number of recoiling protons per unit energy $N_p(E')$ with $E' > E$ produced in slabs dx between Z_1 and Z_2 is related to the number of recoil protons per unit energy loss in the crystal, $N_p(E)$, by $N_p(E) = N_p(E')(dE'/dE)$. Therefore, the ideal recoil-proton spectrum with its distortion produced by the loss of protons through the end of the crystal is given by

$$N'_p(E) = (1/E_o)[N_o A n_h \sigma_h(E_o)(L - Z_1) f(a, L - Z_1)] +$$

$$(1/E_o)[N_o A n_h \sigma_h(E_o)] \int_{L-Z_2}^{L-Z_1} e^{-ax} \, (\partial E'/\partial E) \, dx. \qquad (2\text{-}13)$$

If the range of a proton of energy E in the crystal is approximated by $R(E) = KE^2$, where K is a proportionality constant, and if it is assumed that the fraction of the energy lost in the crystal E/E' is equal to the fraction of the range traversed $r/R(E') = Z/\cos\theta \; R(E')$, then, as in Appendix 4, Eq. (2-13) can be reduced to another equation quoted by Schwartz, Owen, and Ames (7) in their Appendix IV:

$$N'_p(E) = N_p(E) \left\{ 1 + (R_o/L)[(2/5) - (7/5)(E/E_o)^{5/2}] \right\} \qquad (2\text{-}14)$$

Using this equation the recoil-proton spectrum distorted by the loss of protons through the end of the scintillation crystal has been calculated for incident 8.0-MeV neutrons and is shown in Fig. 2.7b. The total number of recorded protons is, of course, not affected by this distortion, but the energy distribution is increased at low energies and depressed at the higher energies. Equation (2-14) indicates that the distorted spectrum is depressed most at $E = E_o$ by the fraction R_o/L, but it equals the ideal spectrum $N_p(E)$ at $E/E_o = 0.6$ or for 8.0-MeV neutrons at 4.8 MeV.

In the same way that protons produced within a distance Z_1 of the end of the crystal do not lose all their energy inside the crystal, those protons produced within some distance S of the edge of the crystal will also not lose all their energy inside the crystal. With the aid of Fig. 2.6, it can be seen that the distance S is given by $R(E) \sin\theta$. The approximations mentioned above, are used in Appendix 4 to show that

UNCLASSIFIED

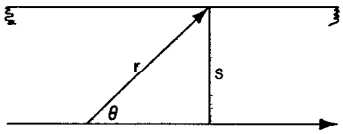

Fig. 2.6—Diagram for deriving the effect of proton loss through the sides of a cylindrical scintillator.

$$S = KE^2 [1 - (E/E_o)]^{1/2}. \tag{2-15}$$

The distance S can be written in terms of $R(E_o)$ as

$$S = R(E_o)(E/E_o)^2 \; [1 - (E/E_o)]^{1/2}.$$

Its maximum value occurs when $E = 0.8E_o$ and is zero when $E = E_o$. For incident neutrons of 8.0 MeV in energy, S is maximum for 6.4-MeV protons and has a value of 0.2862 $R(E_o)$. From the range of 8-MeV protons in stilbene given by Brodsky (8) as 79.65 mg/cm^2 and with the density being 1164 mg/cm^3, S_{max} for E_o = 8.0 MeV is 0.2 mm. If one considers a uniform flux on a crystal 1-inch in diameter, the ratio of the area of the ring of width $r - S_{max}$ to the total cross-sectional area is 0.03125 or 3.125%. The average value of S is approximately $S_{max}/2$ and as one half of the scattering occurs inwardly, the number of protons that leave the sides of the crystal are less than 1/4 of those scattered in a ring of width $r - S_{max}$. Hence, less than 0.8% of the recoil protons in a 1-inch-diameter crystal escape through the sides for an incident neutron energy of 8 MeV.

No analytical expression has been derived to describe this small effect, but the recoil-proton energy spectrum should not be affected at $E = E_o$ while being depressed most in the region $E = 0.8\,E_o$. At the lower energies the spectrum will be increased because of the contributions due to protons that escape the crystal. This effect is independent of the length of the crystal and depends only upon the radius and E_o.

2.4(c) Elastic Scattering from Carbon

The formula for the efficiency of the recoil proton detector, Eq. (2-2), is based upon the assumption that neutrons scattered from carbon atoms are lost from the scintillator. This, however, is true only to a first approximation since these neutrons can still participate in a proton scattering event. The energy of the neutrons scattered elastically from carbon nuclei is given by $E_n = E_o\ (0.858 + 0.142 \cos \alpha)$, where α is the angle of scattering in the c.m. system. Therefore, the energy of the neutrons range from $0.716E_o$ to E_o. As discussed in Appendix 1, the energy spectrum of the scattered neutrons in the laboratory system is determined by their angular distribution in the c.m. system. An examination of the differential scattering cross sections in this system indicates that neutrons with energies greater than 5.0 MeV are scattered primarily in the forward direction (8,9).

As shown by Eq. (A1-29), the energy spectrum of neutrons scattered elastically from carbon atoms is given by

$$(dN_n/dE)_c = [2\pi N_o n_c \sigma_c(E_n,E_o) L f(aL)]\,/0.142E_o. \tag{2-16}$$

These neutrons produce a recoil-proton energy spectrum in a scintillator of area A, expressed in integral form as

$$N_{pc}(E) = \int_{o}^{E_o} A(1/E_n)[n_h \sigma_h(E_n) L' f(aL')]\,(dN_n/dE)_c dE_n. \tag{2-17}$$

In these formulas, E_n represents the energy of the scattered neutrons and L' represents the effective path length for these neutrons inside the scintillator. The differential-elastic-scattering cross section is represented by $\sigma_c(E_n,E_o)$. The recoil-proton energy spectrum produced by these neutrons is flat from zero up to $0.72E_o$ and then decreases to zero at $E = E_o$. Therefore, the neutron-energy spectrum calculated from the distorted recoil-proton spectrum will show two broad groups between $0.72E_o$ and E_o. The variation in amplitude within this energy range reflects the angular distribution in the c.m. system of the neutrons scattered from carbon nuclei. Because of the peaks in the elastic scattering cross section, the magnitude of this effect will vary markedly with the energy of the incident neutrons. The effective length L' may also be a function of energy.

To demonstrate the effect of this scattering, the ideal spectrum with this distortion was calculated for 8.0-MeV neutrons and is shown in Fig. 2.7c. For this calculation, the differential scattering cross section in the c.m. system was taken from values tabulated by Garber et al (9). The effective length of the crystal L' was arbitrarily selected as $L/2$.

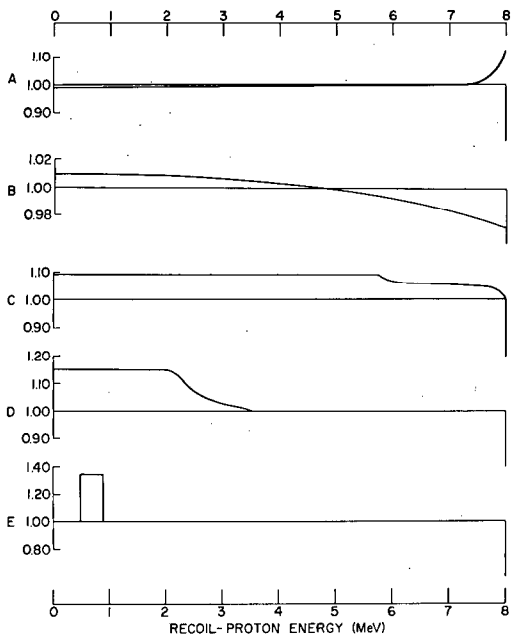

Fig. 2.7—Perturbations to the ideal recoil-proton energy spectrum for 8-MeV neutrons produced in a 1-inch-diameter-by-1-inch long stilbene crystal by (a) escape of protons through the end of the scintillator, (b) neutrons which have two scattering collisions with protons, (c) neutrons which scatter elastically from carbon before producing a recoil proton, (d) neutrons which scatter inelastically from the 4.43-MeV level of C^{12} before producing a recoil proton, (e) alpha particles produced by the $C^{12}(n,\alpha_o)Be^9$ reaction (scintillation pulses in terms of equivalent proton energy). Note changes in the scales of the ordinates.

2.4(d) Inelastic Scattering from Carbon

A fraction of the incident neutron beam will be scattered inelastically from one of the excited levels of carbon. In the calculation of the efficiency of the scintillator using Eq. (2-2), it is assumed that these inelastically scattered neutrons are lost from the scintillator,

UNCLASSIFIED

but some of them will also participate in elastic scattering collisions with protons in the scintillator. These inelastically scattered neutrons produce a perturbation in the recoil-proton energy spectrum given by

$$N_{pc*}(E) = \int_o^{E_o} A(1/E_n)[n_h \sigma_h(E_n) L' f(aL')](dN_n/dE)_{c*}\, dE_n \tag{2-18}$$

In this formula, $(dN_n/dE)_{c*}$ represents the energy distribution of the neutrons scattered inelastically from carbon (c.f. Eq. (A1-30)), and L' again represents an effective path length in the crystal for the scattered neutrons. Since the energy of a scattered neutron depends on the angle through which it is scattered, the energy spectrum of the scattered neutrons depends on the differential inelastic scattering cross section in the c.m. system. In the case of 8.0-MeV neutrons scattered from the 4.43-MeV level of carbon, the energy of the scattered neutrons will vary from 2.05 to 3.50 MeV. Figure 2.7d shows the ideal recoil-proton spectrum with the distortion calculated with the assumption that inelastic scattering occurs only from the 4.43-MeV level of C^{12}. The neutron spectrum derived from the distorted recoil-proton spectrum will show a group of neutrons between 2.0 and 3.5 MeV as a result of the inelastically scattered neutrons. Above 8.0 MeV, scattering from the 7.65-MeV level is possible and the energy spectrum will become more complicated. Because of the high probability of producing recoil protons by the low-energy neutrons scattered inelastically from carbon, spectra produced by high-energy neutrons will contain an important distortion in the low-energy region from this effect.

2.4(e) Alpha-Producing Reactions

Alpha particles can be produced in an organic detector by two reactions, $C^{12}(n,\alpha)Be^9$ and $C^{12}(n,n')3\alpha$. The threshold of the first reaction is about 6.2 MeV and the cross-section peaks at 0.08 barns near 8 MeV (10). The Q value of this reaction is −5.7 MeV so that the energy of alpha particles produced by 8-MeV neutrons will be less than 2.3 MeV and for 14-MeV neutrons less than 8 MeV (c.f. Appendix 1, Eq. (A1-31)). Reference to Fig. 2.4 shows that alpha particles of energy less than 8 MeV produce pulses less than 3-MeV proton equivalent. Therefore, the energy spectrum of recoil protons for 14-MeV neutrons will not be distorted above 3 MeV by pulses due to alpha particles. The alpha particles will produce a peak in the lower energy region of the pulse-height distribution. The energy spectrum of the alpha-particles dN_α/dE is discussed in Appendix 1.

The energy of the recoiling Be^9 nuclei will also be imparted to the crystal simultaneously with the energy of the alpha particles. Therefore, the light output of the scintillator will be the sum of the light produced in each scintillation. This effect, viewed as a distortion of the ideal proton distribution, is shown in Fig. 2.7e for 8-MeV incident neutrons. For simplicity, the energy distribution within the peak is assumed uniform. The effective threshold of the second alpha-producing reaction is 8 MeV, and the energy shared by the three alphas will produce a broad peak in the pulse-height distribution. This peak might be mistaken as being due to low-energy protons.

2.5 Interpretation of Perturbations

All the effects discussed in the preceding section will contribute to the distortion of the ideal recoil-proton energy distribution $N_p(E)$. To determine the magnitude of these effects on the ideal spectrum, the perturbations calculated in the preceding section were added to the ideal spectrum. The resulting distorted spectrum is shown in Fig. 2.8. For comparison, the recoil-proton spectrum calculated from the pulse-height distribution produced by 8.0-MeV neutrons incident on a 1-inch-by-1-inch stilbene crystal is shown in Fig. 2.8. The recoil-proton energy spectrum was obtained by correcting the pulse-height distribution for the nonlinear response of the detector as described in Section 2.3. For this comparison, the ideal spectrum was calculated for the same number of neutrons as were incident upon the detector. This flux was 1.925×10^6 neutrons/cm^2 from a measurement of monoenergetic neutrons which will be discussed in Chapter 4. As can be seen from this graph, the effect of the perturbations is to generate a significant group of recoil protons below 3 MeV, although not enough to explain the experimental data. Some disagreement between calculated and measured spectra is to be expected for a number of reasons. Since the effective length of the crystal for inelastically scattered neutrons must be approximated, the calculations cannot be precise; also no distortion was included for loss of protons through the sides of the crystal. This distortion would also serve to increase the number of low-energy protons and depress the spectrum around 6 MeV. The experimental data also include neutrons scattered from the scintillation counter assembly. The inelastically scattered neutrons from this source will further increase the recoil-proton spectrum at low energies.

At present no reliable procedure has been developed which can be used to remove all the effects of these perturbations from the neutron spectrum as derived from a distorted recoil spectrum. For monoenergetic spectra it may be possible to identify the effect produced by each perturbation and to discount it in the interpretation of the data. However, continuous neutron energy spectra are not so easily interpreted. Broek and Anderson (5) have developed a correction factor which removes most of the effects of second scattering and the loss of protons through the end of the detector. Their expression will be discussed in the next chapter in the section on data analysis.

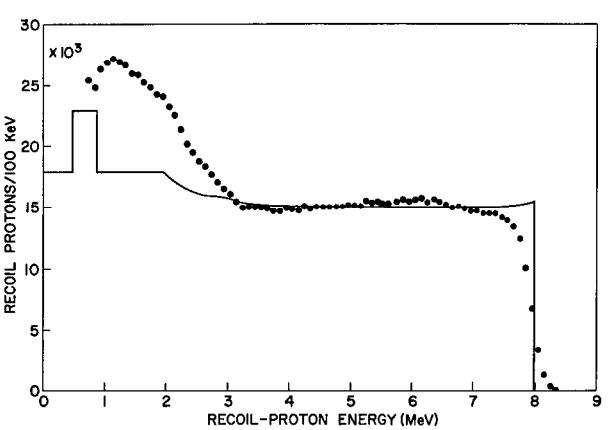

Fig. 2.8—Recoil-proton energy spectrum, shown as curve, calculated with sums of distortions for 8.0-MeV neutrons incident upon a 1-inch-by-1-inch stilbene crystal. Experimental data are shown as the dots. In each case the flux was 1.925×10^6 neutrons/cm^2.

UNCLASSIFIED

3. DATA ANALYSIS AND COMPUTER CODE

3.1. Data Analysis

In this chapter is described a method of analysis for converting pulse-height data, produced by recoil protons in a scintillation detector, to neutron spectra. This analysis is much simpler than the widely used matrix or Monte Carlo methods. It includes corrections for second scattering of neutrons by hydrogen and for loss of protons through the end of the detector. The computer code was originally developed for a small computer which had a 30-bit, 4096-word memory; hence, the code can be adapted for use with comparable computers, such as 16-bit minicomputers, small enough for field use. However, for the sake of clarity the program is presented here in FORTRAN IV compatible with a CDC 3800 computer.

In Chapter 2, the basic concepts concerning pulse-height data from a scintillator due to recoil protons have been discussed. Certain characteristics of the detector have been described as causing perturbations on the ideal recoil-proton energy spectrum. To obtain a recoil-proton energy spectrum from which to derive a neutron spectrum, the pulse-height distribution must be corrected for the nonlinear response of the detector. Since the scintillator was calibrated in terms of proton energy vs electron energy for equal pulse height, the response function expressed in Eq. (2-9) is used. For this spectrometer, it is

$$P = 0.150E^{1.5414} \tag{3-1}$$

where P is the electron energy and E is the proton energy. Values of P for 0.1-MeV energy intervals of E are listed in Appendix 5. Calibration of the pulse-height analyzer with gamma-ray sources relates the electron energy P of the Compton edge E_c defined in Eq. (2-10) to the channel number k by

$$P = a + bk. \tag{3-2}$$

For each pulse-height distribution the constants a and b are obtained from a least-squares fit to the gamma-ray calibration data. The computer program uses stored values of Eq. (3-1) together with Eq. (3-2) to relate channel numbers to proton energies. It then sums over channels to obtain protons per energy interval as here described. Let the channel number corresponding to the lower limit of a proton energy interval be designated k_s, and the one for the upper limit designated k_t. As these are generally noninteger, let $k_s = i_s + f_s$ and $k_t = i_t + f_t$ to separate the integer and fractional values for each limit number. By letting the numbers of counts per channel be designated N, the number of protons in an energy interval N_p is given by

$$N_p = (1 - f_s)N_{i_s+1} + N_{i_s+2} + \ldots\ldots + N_{i_t} + (f_t)N_{i_t+1}. \tag{3-3}$$

Equation (2-5) relates the neutron spectrum to the proton spectrum. With the shape-correction factor B included, the neutron flux dN_n/dE can be expressed as the product of a spectrum conversion function $\psi(E)$ with the negative of the slope of the proton spectrum

defined as $-q/\Delta E = dN_p(E)/dE$, at the center of the corresponding neutron energy interval ΔE:

$$dN_n/dE = \psi(E)(-q/\Delta E), \tag{3-4}$$

with $\psi(E) = E/A\epsilon_n B$. In the expression for $\psi(E)$, E is the neutron energy, A is the cross-sectional area of the detector, B is the shape-correction factor, and ϵ_n is the efficiency for neutron detection by means of recoil protons as expressed in Eq. (2-2). This expression contains neutron cross sections for hydrogen and carbon. For the latter, tabulated values of the total cross section (10), were used, and for the neutron-proton scattering cross section the formulation given by Schwartz, Owen, and Ames (7) as the sum of two terms was used. The first term is 1/4 of the singlet interaction while the second term is 3/4 of the triplet interaction. The expression in barns is

$$\sigma_h = 5.603\pi/(1 + 7.417E + 0.1105E^2) + 0.8652\pi/(1 + 0.2427E + 0.0028E^2) \tag{3-5}$$

with E expressed in MeV. The products of the number of atoms of hydrogen and carbon per cm^3 of stilbene with their respective cross sections, $n_h\sigma_h$ and $n_c\sigma_c$, are listed in columns 3 and 4 of Appendix 5. The values of neutron efficiency ϵ_n for three lengths of stilbene are listed in Appendix 6 and are graphed in Fig. 3.1. The deviations from a smooth curve are due to fluctuations in the carbon cross section. For short crystals, up to 1/2 inch, these fluctuations are negligible. As the graph indicates, the effect of the carbon cross section is increasingly pronounced with increasing length. To understand this, the expression for ϵ_n can be written as

$$\epsilon_n = (n_h\sigma_h/a)(1 - e^{-aL}), \tag{3-6}$$

which shows that the length dependence is only in the exponential term.

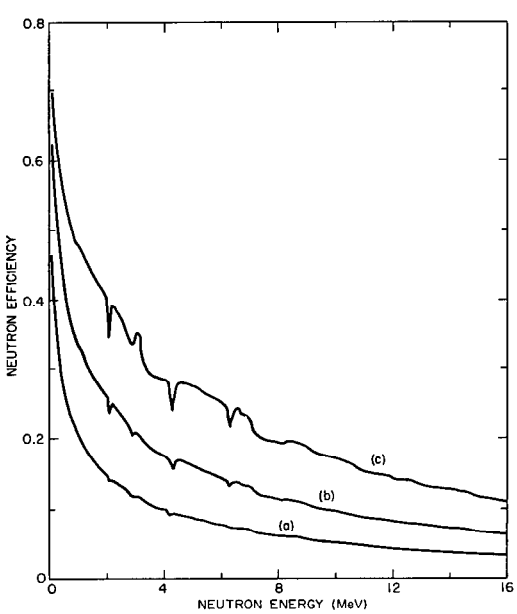

Fig. 3.1—Neutron efficiency ϵ_n given by Eq. (3-6) as a function of energy for stilbene crystals of lengths: (a) 1/2 inch, (b) 1 inch, and (c) 2 inches.

UNCLASSIFIED

The shape-correction factor B, given by Broek and Anderson (5), removes most of the effects of second scattering of neutrons by hydrogen and the loss of recoil protons through the end of the crystal. It may be written as

$$B = 1 - 0.780(R_m/L) + 0.090 n_h \sigma_h L + 0.077 n_h \sigma_h{}' r, \tag{3-7}$$

where $\sigma_h{}'$ is the value of σ_h at $0.068E$. In the second term, which corrects for the escape of protons through the end of the crystal, L must be in the same units as R_m, the range of a proton that receives the full neutron energy. In the third and fourth terms, which correct for second scattering, L and r, the radius, are expressed in centimeters. For stilbene, Brodsky (8) gives $R_m = 1.780(E - 0.119)^{1.815}$ mg/cm^2. The coefficients in the expression for B were obtained by Broek and Anderson by correcting at 90% of full pulse height the distortion caused by the end effect and by second scattering by hydrogen. The magnitude of the neutron peak derived from a pulse-height distribution produced by monoenergetic neutrons is corrected by this factor.

The spectrum conversion function $\psi(E)$ from Eq. (3-4) is tabulated in Appendix 6 for 1-inch-diameter crystals of lengths for which the neutron efficiencies are listed and also for a crystal 3/2-inches in diameter and 1 inch long. This crystal has a volume only slightly larger than that of the 1-by-2-inch crystal; hence, a comparison of the ψ-function values for these two crystals illustrates the dependence of $\psi(E)$ on the crystal shape.

To select an optimum method for calculating the slope of the recoil-proton energy spectrum, various formulations were used. Early calculations showed that it was possible to standardize on a neutron-energy bin width ΔE of 100 keV. It was found that resolution could be maintained and statistical accuracy improved by omitting, in the calculation of the slope, the numbers of protons in energy bins on each side of the neutron energy. If we let the numbers of protons in energy bins from the neutron energy be labeled P_1, P_2, P_3, and P_4 toward increasing energy and P_{-1}, P_{-2}, P_{-3}, and P_{-4} toward decreasing energy, five formulations for the slope and its uncertainties are

$$-q_2/\Delta E = (P_{-2} - P_2)/3\Delta E \qquad \delta_2 = (P_{-2} + P_2)^{1/2}/3\Delta E$$

$$-q_3/\Delta E = (P_{-3} - P_3)/5\Delta E \qquad \delta_3 = (P_{-3} + P_3)^{1/2}/5\Delta E$$

$$-q_4/\Delta E = (P_{-4} - P_4)/7\Delta E \qquad \delta_4 = (P_{-4} + P_4)^{1/2}/7\Delta E$$

$$-q_{23}/\Delta E = (P_{-3} + P_{-2} - P_2 - P_3)/8\Delta E \qquad \delta_{23} = (P_{-3} + P_{-2} + P_2 + P_3)^{1/2}/8\Delta E$$

$$-q_{34}/\Delta E = (P_{-4} + P_{-3} - P_3 - P_4)/12\Delta E \qquad \delta_{34} = (P_{-4} + P_{-3} + P_3 + P_4)^{1/2}/12\Delta E$$

Tests with actual data verified that for $-q_2/\Delta E$ the greater resolution is more than offset by greater statistical fluctuation. For $-q_3/\Delta E$ and $-q_4/\Delta E$ the resolution decreased while the statistical fluctuations also decreased. For $-q_{23}/\Delta E$ and $-q_{34}/\Delta E$ the resolutions were approximately equivalent to those for $-q_3/\Delta E$ and $-q_4/\Delta E$ respectively while the statistical fluctuations were significantly less. The formulation for $-q_{23}/\Delta E$ was chosen over that for $-q_{34}/\Delta E$ as the improved resolution was more important than a slight decrease in statistical uncertainties.

As discussed earlier, scintillation neutron spectrometers must incorporate a means of distinguishing between pulses due to neutrons and those due to gamma rays, either by time-of-flight separation or by pulse-shape discrimination. Even with PSD circuitry, there remains the problem of pile up of gamma-ray pulses. In some cases, such as detection of neutrons from photonuclear reactions, the detector must be shielded with lead to decrease the gamma flux. The efficiency of such detectors for gamma rays as well as for neutrons is important in choosing the length of the detector. A study (11) has been made of the efficiencies as a function of length for various energies and of the effect of size and shape upon the correction factor B and the spectrum-conversion function ψ. The graphs of gamma-ray and neutron efficiencies for stilbene are shown in Fig. 3.2.

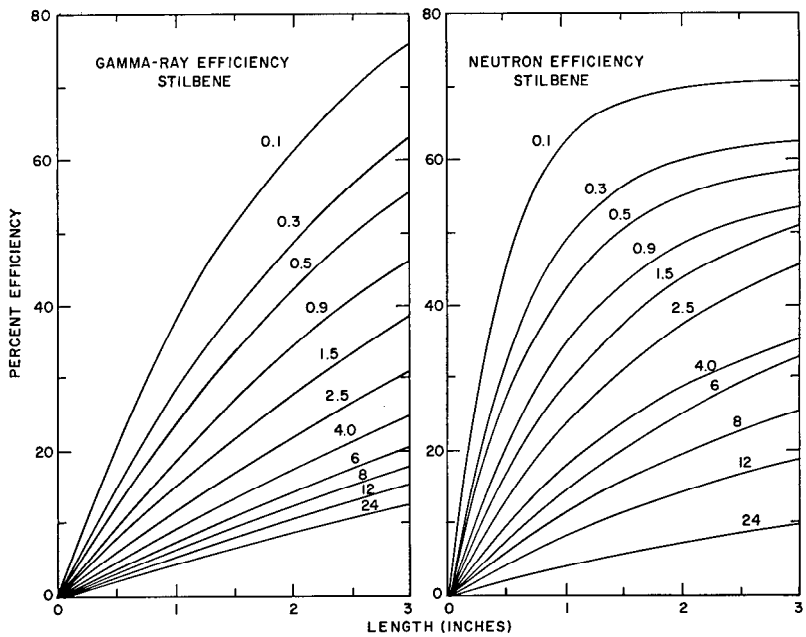

Fig. 3.2—Gamma-ray and neutron efficiencies for stilbene for energies from 0.1 to 24 MeV.

3.2. Computer Code

The FORTRAN code, listed in Appendix 7, processes, in 0.1-MeV intervals, pulse-height data from a 1024-channel analyzer to obtain neutron spectra up to 16 MeV. The 160 values for P, listed in Appendix 5, are designated PTAB. Likewise the 160 values of ψ, appropriate to the detector being used, are designated PSI. Another input is a control labeled KEY which designates the number of data sets (up to 9) which are to be combined. For each data set, DATA(I), a title card and values of A and B from the gamma-source calibration are required. Storage is provided for the proton energy spectrum PROT, the neutron spectrum SPEC, and its uncertainty, DEL. As seen in Appendix 8, the title, the calibration values, and the heading of the output table are printed. If KEY is greater than 1, a new output table is printed for each summing process.

UNCLASSIFIED

Calculations begin with the DO 50 statement. The calculation loop is set for a maximum of 159 cycles to correspond with the maximum neutron energy of 16.0 MeV. The values of P corresponding to the current E and $E + 0.1$ are obtained from the P table and used with A and B to find the lower and upper channel numbers, designated $C1$ and $C2$. If $C1$ is negative or zero, the loop recycles for a new $E = E + 0.1$. The number $C2$ is tested for being greater than 1024 and when this occurs the loop is terminated. When $C1$ is positive and $C2$ is less than 1024, the calculation continues by obtaining the sum of the protons for that energy bin. As $C1$ and $C2$ are generally noninteger, the sum is obtained as follows: (a) the integer part of $C1$, $L1$, is increased by one and designated $D1$ and the fraction $F1$, given by $D1 - C1$, multiplies the number of proton pulses in channel $D1$; (b) the integer part of $C2$, $D2$, plus one gives the channel number for the number of proton pulses to be multiplied by the fraction $F2 = C2 - D2$; (c) to the numbers found in steps (a) and (b) are added the number of proton pulses in the channels from $D1 + 1$ through $D2$. This sum of the protons in the energy interval E to $E + 0.1$ is stored as *PROT(J)* and in a working energy bin. The first value is stored in the bin labeled $PP1$, the second one in $PP2$, and the third and subsequent ones in $PP3$. The first three entries in the table (Appendix 8) give the lower limit of the proton energy, the lower channel number, and the numbers of protons in the 0.1-MeV energy bin. When fourth and subsequent protons sums are obtained, the values in the bins are shifted toward $PM3$ before the currently calculated value is placed in $PP3$. After the sixth sum is found, $PM3$ contains the first sum and the first neutron flux value can be obtained. The negative slope $-q$ is found as $(PM3 + PM2 - PP2 - PP3)/8$. It is designated *QNEG* in the program and is listed in the output table. The neutron flux value, designated *SPEC(K)*, is obtained by multiplying $-q$ by the value of ψ at the central energy E and dividing by ΔE (0.1 MeV in the program). The statistical uncertainty, designated *DEL(K)*, is obtained by substituting for $-q$ its uncertainty, i.e. $(PM3 + PM2 + PP2 + PP3)^{1/2}/8$. These two values are listed in the output table under NEUT and DEL. After the looping is completed, the last two values of E, the channel number, and the number of protons are printed. Sums of protons *PROT(J)* and neutrons *SPEC(K)* having energies in the ranges 4.0 to 6.9, 7.0 to 10.9, and 4.0 to 10.9 MeV are found and printed. Limits on these sums were chosen for a photonuclear experiment and can be modified easily to suit any experiment.

Besides the tabular output, provision is made for punching the neutron-flux values and their uncertainties on cards. The input CID is a card identifier of four characters. Eight values of neutrons are punched on a card with the CID and a card number and likewise for the uncertainties. This computer analysis together with a discussion of its advantages and limitations has been described elsewhere (12).

3.3 Programming for a Small Computer

Features concerning the original code for the data analysis of this chapter will be given only as a guide. Some suggestions are made for modifications to conform to the requirements of newer and faster small computers. The data analysis was first programmed for a Librascope General Precision computer which had a word length of 30 bits, LGP-30. It had a magnetic-drum memory consisting of 64 tracks and 64 words each or a total memory of 4096 words. Fixed-point, machine-language programming was used together with certain subroutines. The more standard word length of 16 or 18 bits in recent computers may make double-precision or floating-point arithmetic necessary so that, in general, double the number of words of memory should be sufficient.

For the LGP-30, a Program Input Routine (3 tracks), which interprets simplified machine-language programming, is used for reading in the program, subroutines, and tables. Subroutines used by the program were a Square-root Routine (1 track), Data Input (0.5 tracks), and a Data Output Routine (4.5 tracks) used for printing the output table. Two additional subroutines were stored on the drum, the Hexidecimal Print and Punch (5-tracks) used for making data output tapes and the Decimal Memory Print (4 tracks) used for diagnostic purposes. With one track assigned for storage for subroutines, a total of 19 tracks were kept constant for this data analysis. The 1024 items of pulse-height data occupied another 16 tracks. The P table and the ψ table needed 160 locations each for a total of 5 tracks. Storage needed for program-generated quantities amounted to 12.5 tracks (2.5 tracks each for the proton spectrum, the neutron data spectrum, its uncertainties, the neutron background spectrum and its uncertainties). The program itself including working storage fitted into 9.5 tracks. This left only two tracks not utilized.

Without the Decimal Memory Print and the separate storage for the background neutron spectrum and its uncertainties, there would have been 11 tracks not utilized. The separate locations for background and data were needed for the photoneutron experiment as will be explained in Section 4.3. Tapes of the data and background spectra made using the Hexidecimal Print and Punch permitted the spectra to be read back into the same locations for further processing by an additional program.

Programming in machine or assembly language rather than a compiler language saves memory space and time for execution; both features were important for the LGP-30 computer. Maximum use of looping, sense switches and subsections, such as a section for clearing 160 locations, was made in the LGP-30 program to minimize the program length. For newer, faster computers a section to calculate P might occupy less space than that needed for the P table.

The FORTRAN code, listed in Appendix 7, can be used as a guide for determining the various steps and looping processes needed for this type of data analysis. The individual small computer may have features that simplify certain procedures when machine-language programming is used. As an example, the process of separating the integer and fractional parts of the calculated channel numbers was easily accomplished using an extract order with an appropriate mask.

4. EXAMPLES OF DATA ANALYSIS

4.1. Monoenergetic Neutron Spectra

A good test of both the equipment and the method of analysis is performed when the energy spectrum of a monoenergetic beam of neutrons is measured. For this purpose a deuterium target was bombarded by deuterons accelerated to 4.754 MeV by the NRL Van de Graaff. The deuteron target was 40-keV thick so that a nearly monoenergetic beam of neutrons, 8.0 ± 0.025 MeV, was produced at zero degrees. The detector described in Chapter 1 was oriented such that the neutrons were incident normally upon the face of a cylindrical stilbene crystal 1 inch in diameter and 1 inch long.

UNCLASSIFIED

The pulse-height data, collected in 1024 channels, were analyzed by the method described in the preceding chapter. The derived neutron spectrum is shown in Fig. 4.1 where the fwhm of the peak, centered about 8 MeV, is 500 keV. This value indicates that, after taking out the effect of energy spread of the neutrons from the target, the overall resolution of the system was 430 keV at 8 MeV. The computer output for the analysis of these data is given in Appendix 9, where it can be seen that at channel 600, 100 keV of proton energy corresponds to 14 channels of pulse-height data. As the usefulness of this spectrometer depends upon the accuracy with which the energy scale is defined, the energy drift must be contained within a single 100-keV bin. This equipment provides the required stability of ±7 channels at channel 600 by having an overall drift of ±1%*.

The spectrum, produced by 8-MeV incident neutrons, was obtained by using the computer code previously described which included corrections for second scattering by hydrogen and for loss of protons through the end of the scintillator. As no corrections were made for the other perturbations discussed in Chapter 2, this computer analysis permits the observation of these effects, namely, the appearance of groups of neutrons in the spectrum between 6.0 and 7.5 MeV and between 2.0 and 3.5 MeV. In view of the discussion in Chapter 2, the first group immediately below the peak is considered to be due to neutrons elastically scattered with carbon before producing recoil protons. The energy range of the lower energy group is that which was predicted for inelastically scattered neutrons from the 4.43-MeV level of carbon. The magnitude of this group is 184,860 neutrons/100 microcoulombs compared with 1,849,000 neutrons/100 microcoulombs in the main peak at 8 MeV (the numbers for the lower energies were made symmetric with the high-energy tail). If the effective length for neutron-proton scattering after a scattering from carbon is taken to be $L/2$ and the average value of the scattered-neutron energy is used, the ratio of the inelastically scattered neutrons to the full-energy neutrons is calculated to be 0.06 compared with 0.10 from the measured peaks. The discrepancy between these ratios indicates that additional neutrons appear in the measured spectrum. These neutrons could be derived from additional inelastic scattering reactions with the material surrounding the scintillator which is composed primarily of aluminum. No attempt has been made to estimate the effect of these reactions.

An additional test of the method of analysis is obtained by comparing the number of neutrons in the peaks of the derived spectra with the number of neutrons incident on the crystal as calculated from the $H^2(d,n)He^3$ differential cross section at zero degrees and experimental parameters. The neutron flux at the detector position in units of neutrons/cm^2-μC is obtained from

$$F = 3.15 \times 10^5 Pk\sigma(d,n)(1/D^2), \qquad (\pm 10\%) \qquad (4\text{-}1)$$

where P is the pressure in atmospheres, k is the thickness of the gas target, and D is the distance from the center of the gas target to the face of the detector. For this test, the energy spectra of neutrons of 2.0, 4.0, 6.0, and 8.0 MeV were measured using a stilbene crystal 1 inch long and 1 inch in diameter. The neutron spectra derived from these measurements are shown in Fig. 4.2. Similar measurements were made using a 1/2-inch-by-1-inch crystal, and

*In Chapter 1 it was pointed out that an electronic stability of 0.01% was desirable to provide the required stability.

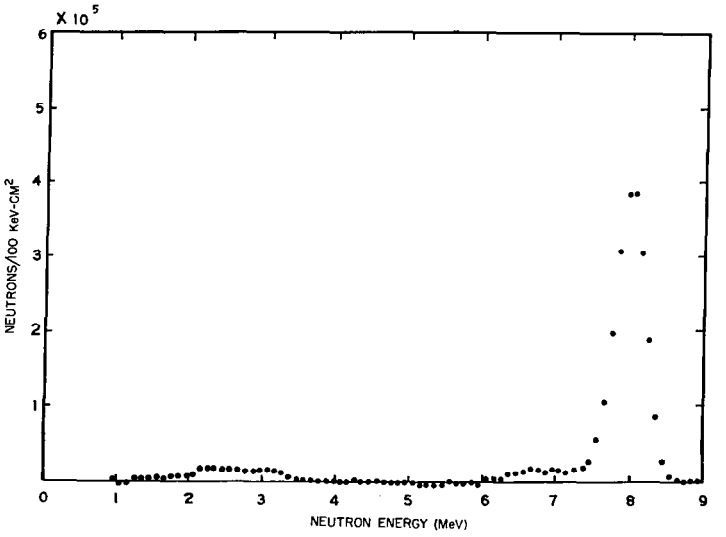

Fig. 4.1—Neutron spectrum derived from the pulse-height distribution produced by a flux of 1.925 X 10^6 neutrons/cm^2 of 8.0-MeV neutrons on a 1-inch-by-1-inch stilbene crystal. This spectrum was derived from the recoil-proton distribution shown in Fig. 2.8, and the computer output of the analyzed data is given in Appendix 9.

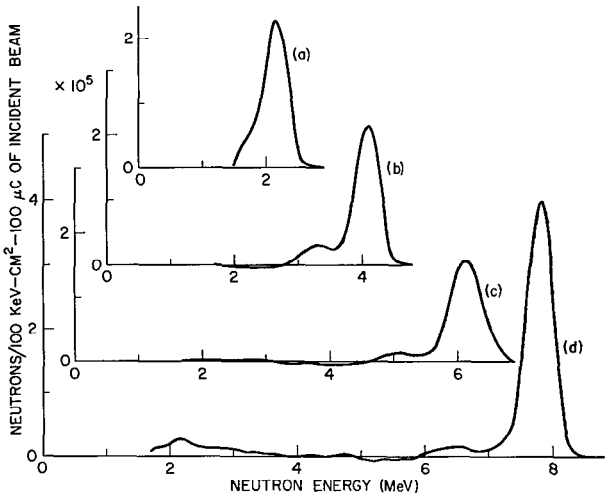

Fig. 4.2—Neutron spectra derived from data obtained with monoenergetic neutrons incident on a 1-inch-by-1-inch stilbene crystal. The spectra are for (a) 2-MeV neutrons, (b) 4-MeV neutrons, (c) 6-MeV neutrons, and (d) 8-MeV neutrons. Note: Spectrum d is not from the same data as that for Fig. 4.1.

the derived spectra are shown in Fig. 4.3. The measured values, based on the peak only (as the code compensates for loss of scattered neutrons), are compared with calculated values for both detectors in Table 4.1. Although the uncertainties in the measurements were not analyzed in detail, the discrepancies show that these uncertainties are about equal to the uncertainties in the calculations of the neutron flux.

UNCLASSIFIED

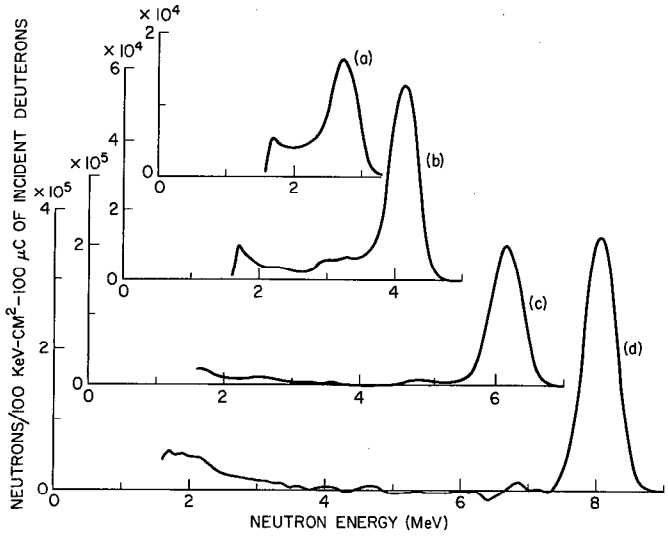

Fig. 4.3—Neutron spectra derived from data obtained with monoenergetic neutrons incident on a 1-inch-diameter and 1/2-inch-long stilbene crystal. The spectra are for (a) 2.7-MeV neutrons, (b) 4-MeV neutrons, (c) 6-MeV neutrons, and (d) 8-MeV neutrons.

Table 4-1
Comparison of Measured and Calculated Neutron Flux

Energy (MeV)	Resolution (keV)	Measured Flux	Calculated Flux	Discrepancy
1-inch-X-1-inch Stilbene				
8.0	478	19804	26760	−26%
6.0	624	10234	12770	−20%
4.0	480	9544	11194	−15%
2.0	500	9541	7774	+23%
1-inch-X-1/2-inch Stilbene				
8.0	568	21767	22530	− 4%
6.0	535	11360	13360	−15%
4.0	440	2586	3443	−25%
2.7	444	757	664	+14%

4.2. Energy Spectra of Neutrons from α-n Sources

The usefulness of this spectrometer for measuring continuous neutron spectra is illustrated by the results of measuring neutrons from a 1-curie *PuBe* source. For this measurement, a 1-inch-by-1-inch cylindrical stilbene detector was placed 30 cm from the neutron source for 2635 minutes. The computer analysis of the pulse-height data is given in

Appendix 8, and the measured spectrum is presented in Fig. 4.4. This spectrum has better resolution than published spectra measured with scintillation spectrometers and processed by other computer codes (c.f. Ref. 12).

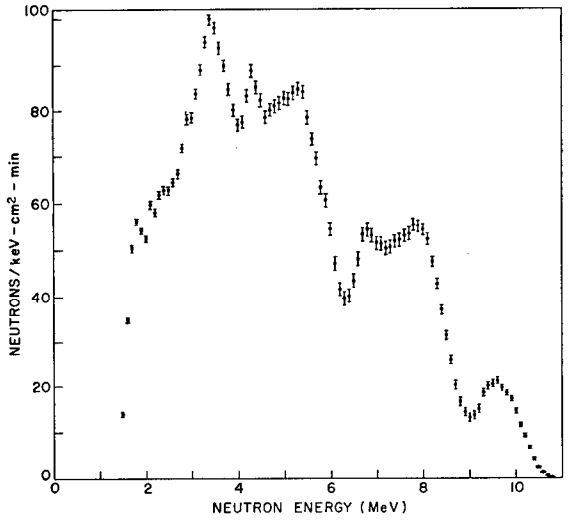

Fig. 4.4— Spectrum of neutrons from a *PuBe* source; the computer analysis of the data is given in Appendix 8.

Neutrons from a *PuBe* source are produced by the $Be^9(\gamma,n)C^{12}$ reaction. For an average alpha energy of 5.14 MeV from *Pu*, this reaction is such that neutrons emitted with energies of 6 MeV or greater leave C^{12} in its ground state, neutrons between 3.3 and 5.9 MeV in energy leave C^{12} in the 4.43-Mev excited state, and neutrons emitted with energies below 2.8 MeV leave C^{12} in the 7.66-MeV excited state. A theoretical calculation by Van der Zwan (13) and the measurement by Rubbino et al. (14), who used a different method of detection, are compared with the NRL measurement in Fig. 4.5. For this comparison, the theoretical calculation and the data of Rubbino et al. were normalized to the NRL measurement of ground state neutrons by normalizing the integral of their values above 6 MeV. As both experimental measurements below 6 MeV are lower than the magnitude predicted theoretically, the indication is that this theory predicts too much excitation of the 4.43-MeV state of C^{12}.

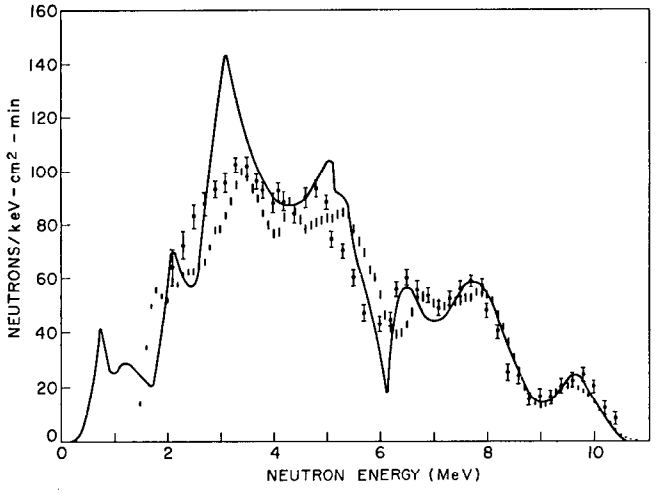

Fig. 4.5—*PuBe* neutron spectra: NRL data (same as Fig. 4.4) shown as the bars indicating the extent of statistical uncertainties, smooth curve is the theoretical calculation by Van der Zwan (13); points with error bars are the data of Rubbino et al. (14). Spectra are normalized to the same value of the integral for data above 6 MeV.

UNCLASSIFIED

The occurrence of peaks in the present measurement at 7.9 and 9.6 MeV is in good agreement with the theoretical predictions, but those at 3.4, 5.4, and 6.7 MeV are somewhat higher than the predicted values. This disagreement may have been introduced by inaccurate γ-ray calibration or an inaccurate value of α in Eq. (2-9) for the electronic system used.

A calibration using neutron moderators and BF_3 detectors at the National Bureau of Standards indicated that 1.38×10^6 neutrons per second were emitted from the *PuBe* source. Integration under the measured spectrum from 2.5 to 10.8 MeV with an adjustment for lower-energy neutrons using Van der Zwan's calculation yields a measured value of 1.3×10^6 neutrons per second, in good agreement with the NBS value.

The energy spectrum of neutrons from an *AmBe* source was also measured, and the derived energy spectrum is presented in Fig. 4.6. The agreement with theory is similar to that for the *PuBe* source. One point to be noted concerning the *AmBe* spectrum is that the dip at 6.1 MeV is shallower than in the *PuBe* spectrum. This is in agreement with the theoretical calculations of Van der Zwan (13).

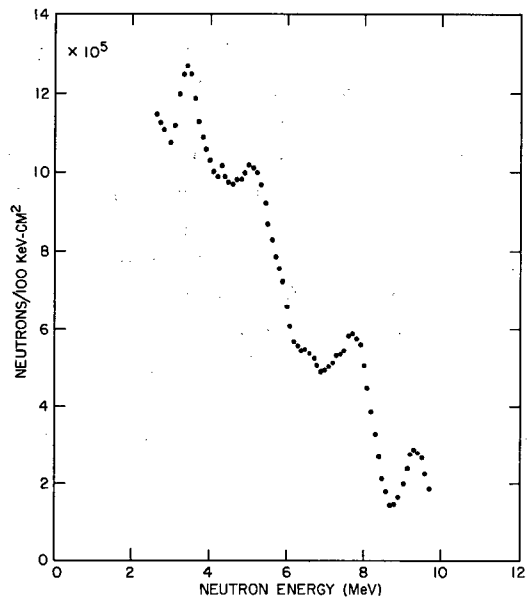

Fig. 4.6—Energy spectrum of neutrons from an *AmBe* source. Since the geometry of exposure was not optimized (as it was for the *PuBe* source, Figs. 4.4 and 4.5), the rise in the spectrum at low energies is due in a large part to scattered neutrons.

4.3. Other Spectra

Besides the measurements just described, this spectrometer has been used to measure two additional spectra: (a) the energy spectrum of neutrons scattered from carbon and (b) the energy spectrum of photoneutrons from the $O^{16}(\gamma,n)O^{15}$ reaction. The energy spectrum of neutrons scattered from C^{12} is shown in Fig. 4.7. For this measurement ring geometry was used with an 18-inch-long brass scattering bar shielding the detector from the 8.0-MeV neutrons produced by a $D(d,n)$ reaction. The scattering ring of carbon was placed such that the scattering angle was 76°, defined by the angle between the line of flight of neutrons incident on the ring and the direction of the detector from the scatterer. In the spectrum, the peak around 6.7 MeV represents neutrons scattered elastically from C^{12}. The peak around 2.7 MeV represents neutrons scattered inelastically from the 4.43-MeV state of C^{12}.

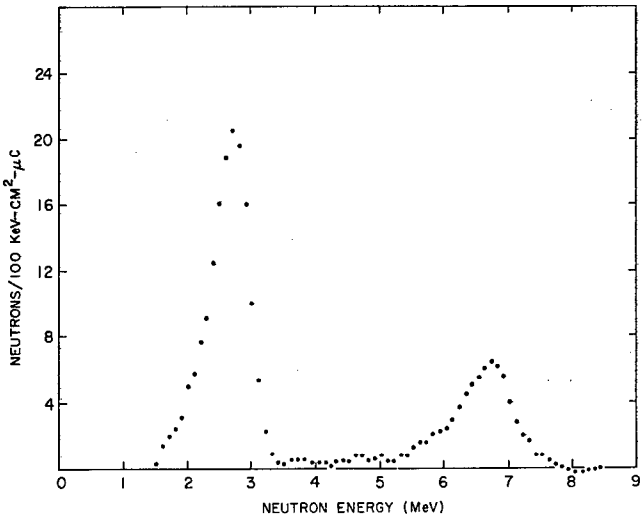

Fig. 4.7—Energy spectrum of neutrons scattered from C^{12}. The peak around 6.7 MeV is produced by neutrons scattered elastically and the peak around 2.7 MeV is produced by neutrons scattered inelastically from the 4.43-MeV level of C^{12}.

In Fig. 4.8 is shown the energy spectrum of photoneutrons from the $0^{16}(\gamma,n)0^{15}$ reaction induced by bremsstrahlung having an end-point energy of 28 MeV. In this spectrum almost all neutrons above 5 MeV leave the resultant nucleus in its ground state. The peak at 6 MeV is due to a peak in the nuclear absorption of gamma rays at 22 MeV. The spectrum was measured with the scintillation detector placed at 90° relative to the direction of the bremsstrahlung beam. The detector was shielded with 3 inches of lead on each side and with 2 inches of lead in the neutron path to prevent pileup of pulses due to gamma rays. The spectrum was not corrected for the absorption of neutrons by the lead in the neutron path but it was corrected for scattered neutrons. A background spectrum was obtained with a polyethylene rod placed in the neutron path. Both the data and background spectra were processed by the original code on the small computer, as described in Section 3.3. An additional program normalized the data and background spectra to the same bremsstrahlung dose and obtained the net spectrum and its uncertainties.

4.4. Uranium Assay

Another application which makes use of the energy resolution of the instrument, but not its full capability as a spectrometer, has been described by Jones et al. (15). They tested a new technique for assaying uranium samples based on the difference in the fission cross sections of various uranium isotopes. In a trial of the method, samples of uranium were bombarded with a beam of 0.5-MeV neutrons obtained from the $H^3(p,n)He^3$ reaction using the NRL 5-MV Van de Graaff. The 0.5-MeV neutrons caused fission in U^{235} but not in U^{238} due to its high fission threshold. The fission neutrons, scattered incident neutrons, and background gamma rays were allowed to strike a stilbene scintillator 1-inch in diameter by 1/2-inch thick, placed approximately 15 cm from the sample and at 90° to the incident beam. For the purpose of this experiment, the number of neutrons above a given energy was taken as proportional to the sum of the recoil-proton pulses above that energy. From the calibration of the spectrometer, as described in Section 2.3, any desired neutron-energy threshold can be selected by summing the counts above a given channel.

UNCLASSIFIED

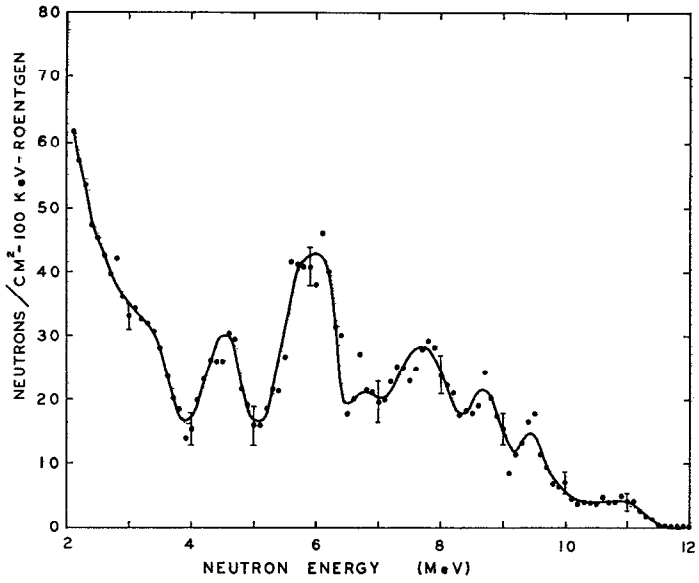

Fig. 4.8—Energy spectrum of photoneutrons at 90° from the $O^{16}(\gamma,n)O^{15}$ reaction induced by 28-MeV bremsstrahlung. No correction has been made for the effect of the lead in the neutron path but correction has been made for scattered neutrons from the lead surrounding the detector.

In Fig. 4.9 are shown the results of a set of runs for which the threshold was set at 1.25 MeV. In this case two 2.1-g samples of U^{235} were added successively to a 191-g sample of depleted U^{238}. The sensitivity and reproducibility, at least for this test geometry, is considerably less than a gram of U^{235}. The authors also discuss other variations of this general technique.

Fig. 4.9—Results of a test of the neutron spectrometer for use in the assay of U^{235} in the presence of a 191-g depleted sample of U^{238}. Neutrons of energy 0.5 MeV were incident on the combined sample. Responses proportional to fission neutrons only are obtained by summing the counts due to recoil protons of energies greater than 1.25 MeV. One unit monitor response (UMR) corresponds to a dose at the sample of $\approx 2.9 \times 10^8$ neutrons/cm^2. This figure is taken from Ref. 15.

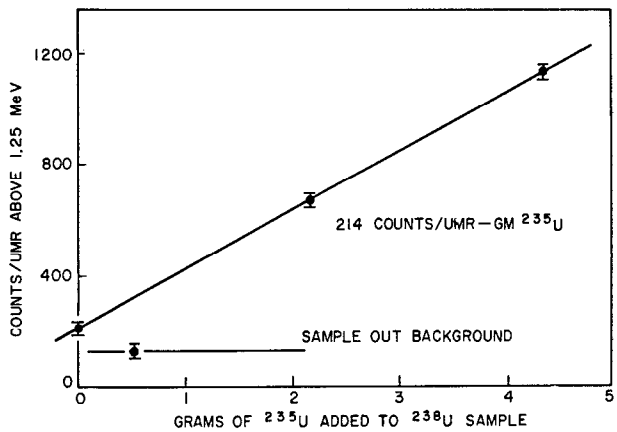

5. PULSE-SHAPE-DISCRIMINATION CIRCUIT

5.1. General Description

Organic scintillation detectors were historically limited in their application to the field of fast neutron spectroscopy by their sensitivity to the gamma-ray flux which always accompanies neutrons. In recent years, however, methods for identifying the particle which induced the scintillation have been developed. Following the methods introduced by Brooks (16) and Owen (17) numerous circuits were presented to identify the particle which induced the scintillation. Owen (18) has prepared a bibliography of the circuits developed up to 1962, and an additional method based on that of Fortè et al. (19) may be found in a paper by Roush et al. (20). These developments together with the development of stable linear amplifiers, pulse-height analyzers, and photomultiplier power supplies have made it possible to construct an electronic system suitable for organic-scintillation-counter spectroscopy. A block diagram of the electronic system developed at NRL is shown in Fig. 1.1 and discussed in Chapter 1. In this chapter the details of the pulse-shape-discrimination (PSD) circuit will be discussed.

Neutrons and gamma rays, in the energy range of 0.1 to 10 MeV, interact with organic crystals primarily by elastic scattering collisions with protons and electrons, respectively. These scattered electrons and protons induce scintillations in the detector. For stilbene and most liquid scintillators, the light pulse emitted during these scintillations may be characterized by a very fast rise, in initial fast decay during which most of the light is emitted, and then a slow, nonexponential decay consisting of several slower components and persisting up to several microseconds (17, 21-23). It has been found that the relative intensity of the slow to fast components increases with increasing ionization density. Early experiments by Owen (17) indicated that for stilbene the ratio of the intensity of the slow components was about 1.8 times larger for proton excitation than for electron excitation. Later experiments by Bollinger and Thomas (22), who used a delayed coincidence method to investigate the pulse shapes, indicate that the ratio should be about 4.5. They also noticed that there may be a significant difference in the decay of the fast components for different ionization densities. Discrimination between pulses induced by neutrons and gammas depends on these differences in the pulse shapes.

Several requirements are placed upon a PSD circuit which is to be useful for neutron spectroscopy: (a) it should be useful for stilbene, *NE*-213, and other possible organic neutron detectors, (b) it should be able to function at a counting rate exceeding an average of 10^5 counts per second, and (c) it should be possible to operate it remotely from the scintillation detector.

Following these design ideas a PSD circuit was developed at NRL based on the principles employed by Brooks and by Owen, but which uses new electronic techniques to reduce the dead time of the circuits and provides discrimination over a range of neutron energies extending from 500 keV to 15 MeV. The PSD circuit is contained in a module of standard dimensions and is designed to be compatible with modular counting equipment. The module, which provides gates to identify both neutrons and gamma rays, accepts a pulse from a remote photomultiplier and has been used with both stilbene and *NE*-213 scintillation detectors.

UNCLASSIFIED

As discussed in Section 1.1, a separate pulse recorded in the pulse-height analyzer is taken from the 11th dynode.

The block diagram of the PSD module is shown in Fig. 5.1, and some waveforms are shown in Fig. 5.2. The scintillation counter used to test this module consisted of a 1/2-inch-long-by-1-inch-diameter stilbene scintillation crystal mounted upon an RCA 6810A photomultiplier. The cathode of the photomultiplier was operated at high voltage (normally 2000 V) so that the anode could be operated at ground potential and connected directly to a length of 50-ohm coaxial cable. To insure current linearity up to 300 mA, it was necessary to use a divider string for the photomultiplier described in Section 1.2. The current pulse from the anode of the photomultiplier is developed across the 50-ohm input to the PSD module which accepts negative pulses ranging from 0 to 15 V in amplitude.

The input is admitted to three branches as shown in Fig. 5.1. In the lowest branch used to produce logic signals, the pulse is integrated to obtain a pulse proportional to the total charge delivered by the photomultiplier and admitted to an amplitude discriminator. The output of the amplitude discriminator triggers three pulse generators: the reset pulse generator, the gate pulse generator, and the oscilloscope unblank pulse generator. The purposes of these pulse generators are, respectively: to reset the waveforms inside the PSD circuit to zero after 1.5 μsec, to gate the output of the PSD circuit at 1.0 μsec, and to unblank the oscilloscope used to monitor the operation of the PSD circuit. The duration of the amplitude discriminator output determines a dead time during which the PSD module will not identify a second pulse. A parallel output of the amplitude discriminator forms a trigger pulse for additional electronic monitors.

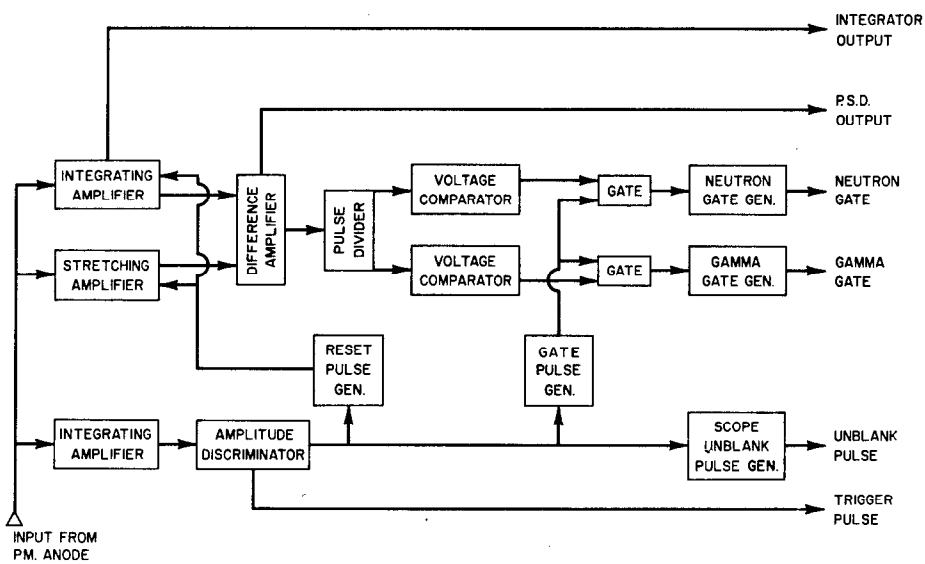

Fig. 5.1—Block diagram of pulse-shape-discrimination module. The "integrator output" shown here is used for oscilloscope monitoring and is distinct from the integrated output of the preamp-amplifier combination shown in Fig. 1.1.

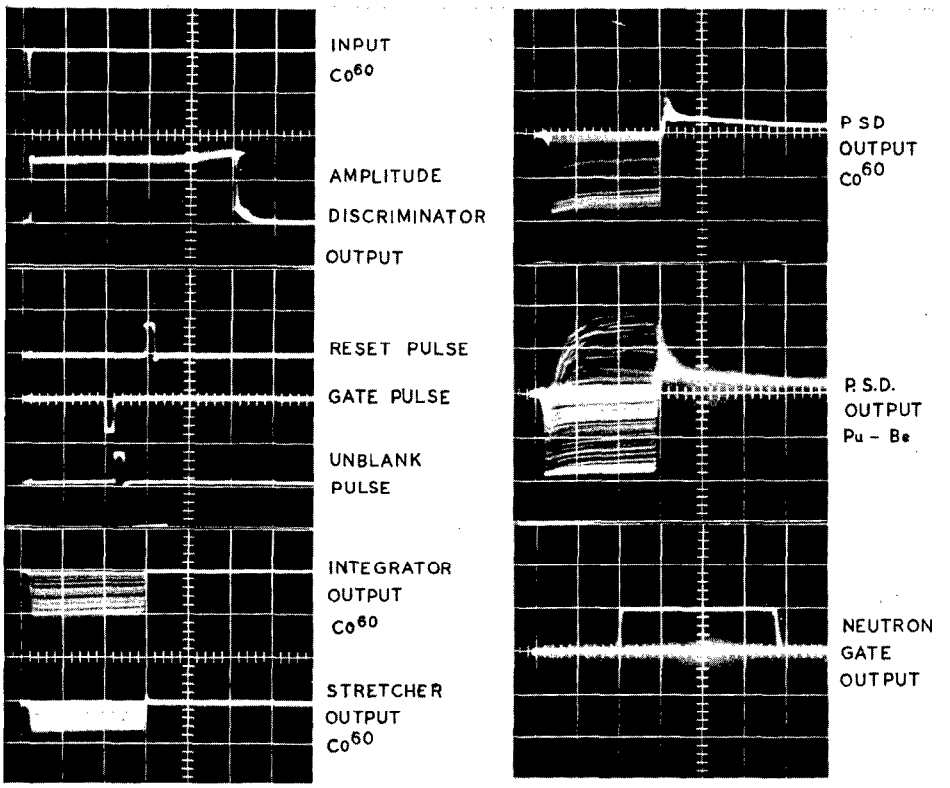

Fig. 5.2—Waveforms in PSD module. The horizontal scale is 0.5 μsec/division.

The three circuits which discriminate between neutrons and gamma rays are the integrating, stretching, and difference amplifiers. The input pulse is simultaneously admitted to the integrating and stretching amplifiers. In the integrating amplifier, the input pulse is integrated to obtain an output proportional to the total charge delivered up to the time the output is measured. In the stretching amplifier the input pulse is differentiated so that the output is proportional only to the charge delivered during the first few nanoseconds of the scintillation. As shown in Fig. 5.2, both these pulses are reset to zero by a pulse from the reset pulse generator at 1.5 μsec. Resetting these pulses to zero reduces the dead time of the discriminator and eliminates the necessity of precisely balancing the long decay times of the integrator and stretcher. The integrated pulse is admitted to the inverting input of the difference amplifier while the stretched pulse is admitted to the noninverting input. Because the total charge delivered during a neutron-induced scintillation is greater than the total charge delivered during a scintillation induced by a gamma ray of the same initial peak current, it is possible to adjust the gain of the integrator to obtain a positive output from the difference amplifier for pulses induced by neutrons and a negative output for pulses induced by gamma rays.

The output of the difference amplifier is passed through a four-diode pulse divider circuit which separates the positive neutron pulses from the negative gamma pulses. Both the neutron output and the gamma output are used to generate gate pulses to identify the

UNCLASSIFIED

respective particle. Before generating these gates, however, the outputs of the pulse divider are admitted to voltage comparators. During the time in which the output of the difference amplifier exceeds the threshold of the voltage comparator, the pulse is standardized to a constant amplitude which is compatible with the logic circuits which follow. The pulse from the voltage comparator is then passed through a logic gate, which is opened only during the time interval specified by a 100-nsec pulse from the gate pulse generator. Since the gate is opened only during this pulse, the output of the difference amplifier is measured at a time specified by the gate. Gating the difference amplifier output precisely defines the time at which the gate pulses to identify neutrons and gamma rays appear. This gating also prevents overshoots at the beginning and end of the difference amplifier output from triggering the pulse generators and, therefore, reduces the effect of a mismatch in rise times and reset times.

The PSD module, therefore, provides logic signals to identify both neutrons and gamma rays. To monitor the operation of the PSD circuit during the course of an experiment, the outputs from the integrating and difference amplifiers are also provided together with a pulse to unblank an oscilloscope. To reduce the time necessary for calibration and inspection of the PSD circuit, all the waveforms shown in Fig. 5.2 are available by means of a selector switch on the front panel. This makes it possible to display any of the waveforms on an oscilloscope which is triggered by an output from the amplitude discriminator. These outputs are connected through 20-dB attentuators.

5.2. Pulse-Shape Discrimination

A detailed diagram of the integrating, stretching, and difference amplifiers is shown in Fig. 5.3. The integrating amplifier ($Q2$ through $Q8$) and stretching amplifier ($Q9$ through $Q14$) are based upon principles described by Larsen (24). These amplifiers are identical except for the time constants of the input networks $R1C1$ and $R4C4$. Consider first the integrating amplifier. The input pulse from the photomultiplier anode is differentiated with a time constant $R1C1$ in the emitter circuit of $Q3$. A current pulse proportional to this derivative is therefore generated in $Q3$. This current pulse is passed through $Q4$ to the storage capacitor $C3$. Transistor $Q4$ is normal off so that there is a small threshold due to the current necessary to turn $Q4$ on. This current, determined by $R7$ and the base emitter voltage of $Q4$, is about 10μA. The differentiating time constant $R1C1$ of the input circuit is about 60 μsec so that the voltage pulse developed on $C3$ is proportional to the total charge delivered during the scintillation pulse. In the stretching amplifier, however, the time constant $R4C4$ is about 60 nsec so that the differentiated pulse swings through zero after about 50 nsec cutting off $Q11$. In this case only the current delivered during the first few nanoseconds charges the storage capacitor, thus "stretching" the peak output of the scintillation pulse. Therefore, the pulse developed across $C3$ represents the integral of the scintillation pulse while the pulse developed across $C6$ represents the current delivered only in the peak of the voltage pulse. The output versus input curves of both these amplifiers have nonzero intercepts because of the small threshold current necessary to turn $Q4$ and $Q11$ on.

Two important characteristics of these amplifiers are: (a) the response curve is linear over a wide range of input currents so that the effect of the threshold current can be made small by choosing the current range large enough; and (b) these two amplifiers are nearly identical, thus reducing the effects of nonlinearity—a problem which has impaired the operation of other PSD circuits at low energies.

UNCLASSIFIED

NRL Report 7324

A Neutron Spectrometer Using Organic Scintillators

D. W. JONES AND M. ELAINE TOMS

Linac Branch
Nuclear Sciences Division

PLEASE RETURN THIS COPY TO:

NAVAL RESEARCH LABORATORY
WASHINGTON, D.C. 20375
ATTN: CODE 2628

Because of our limited supply you are requested to return this copy as soon as it has served your purposes so that it may be made available to others for reference use. Your cooperation will be appreciated.

NDW-NRL-5070/2651 (Rev. 9-75)

LOAN COPY

November 10, 1971

NAVAL RESEARCH LABORATORY
Washington, D.C.

Approved for public release; distribution unlimited.

UNCLASSIFIED

CONTENTS

Abstract iii
Problem Status iii
Authorization iii
Table of Symbols iv

INTRODUCTION 1

1. GENERAL DESCRIPTION OF NEUTRON SPECTROMETER 2

   1.1 Block Diagram of Neutron Spectrometer 2
   1.2 Scintillation Counter 3
   1.3 Pulse Amplifiers and Pulse-Height Analyzer 5
   1.4 Summary and Comment 6

2. PULSE-HEIGHT DATA FROM RECOIL PROTONS 7

   2.1 Introduction 7
   2.2 Neutron-Proton Elastic Scattering 7
   2.3 Nonlinear Pulse-Height Response 8
   2.4 Perturbations of the Ideal Recoil-Proton Spectrum 12
      (a) Second Scattering of Neutrons 12
      (b) Loss of Recoil Protons 13
      (c) Elastic Scattering from Carbon 15
      (d) Inelastic Scattering from Carbon 16
      (e) Alpha-Producing Reactions 17
   2.5 Interpretation of Perturbations 18

3. DATA ANALYSIS AND COMPUTER CODE 19

   3.1 Data Analysis 19
   3.2 Computer Code 22
   3.3 Programming for a Small Computer 23

4. EXAMPLES OF DATA ANALYSIS 24

   4.1 Monoenergetic Neutron Spectra 24
   4.2 Energy Spectra for Neutrons from α-n Sources 27
   4.3 Other Spectra 29
   4.4 Uranium Assay 30

5. PULSE-SHAPE-DISCRIMINATION CIRCUIT 32

5.1 General Description 32
5.2 Pulse-Shape Discrimination 35
5.3 Logic Circuits 39
5.4 Summary and Comment 41

REFERENCES 43

APPENDIXES

APPENDIX 1—Energy Distributions of Reaction Products 45
APPENDIX 2—Summary of Energy Calibrations for Stilbene 50
APPENDIX 3—Derivation for Second Scattering by Hydrogen 51
APPENDIX 4—Derivation of Effects due to Loss of Protons 53
APPENDIX 5—Table of Response Function and Cross Sections 56
APPENDIX 6—Table of Efficiencies and ψ-Functions 58
APPENDIX 7—Listing of Computer Code in FORTRAN 62
APPENDIX 8—Computer Output Table for *PuBe*-Neutron Data 64
APPENDIX 9—Computer Output Table for 8-MeV Neutrons 66

UNCLASSIFIED

ABSTRACT

Organic scintillation detectors are useful for neutron spectroscopy because pulses induced by gamma rays and those induced by neutrons can be distinguished by electronic means. Computer analysis can be used to obtain the energy spectrum of the neutrons from the measured recoil-proton pulse-height distribution. This report describes a practical neutron spectrometer with improved electronic circuitry for pulse-shape discrimination. A detailed study of the interaction of neutrons with the scintillator is presented in relation to pulse-height analysis. A computer program that uses a straightforward method of pulse-height analysis is given in FORTRAN with suggestions for adaptation for use on a small computer. Spectrometer applications are presented for measuring neutron spectra of monoenergetic neutrons, radioactive neutron sources, scattered neutrons and neutrons from a photonuclear reaction and also for detection of fission neutrons.

PROBLEM STATUS

This is a final report on this neutron spectrometer.

AUTHORIZATION

NRL Problem H01-09
Project RR 002-06-41-5005

Manuscript submitted July 8, 1971.

TABLE OF SYMBOLS

N_o	Flux of incident neutrons (neutrons/unit area)
E_o	Energy of incident neutrons (MeV)
A	Area of the detector (cm^2)
L	Length of the detector (generally cm)
N_p	Total number of recoil protons produced in the detector
E	Energy of protons or neutrons (MeV)
$\epsilon(E,L)$	Efficiency of the detector for producing recoil protons (c.f. Sec. 2.2)
n_h	Protons per unit volume of the detector
n_c	Carbon atoms per unit volume of the detector
$\sigma_h(E)$	Neutron-proton scattering cross section
$\sigma_c(E)$	Total neutron interaction cross section with carbon
a	Reciprocal of the absorption length, $a = n_h\sigma_h(E) + n_c\sigma_c(E)$
N	Flux of neutrons within the detector, $N = N_o e^{-ax}$
dE/dx	Rate of energy loss by charged particles in the detector
$R(E)$	Range of proton of energy E in the detector
P	Electron energy (MeV)
dN_p/dE	Recoil-proton flux per unit energy
dN_p/dP	Recoil-proton flux per unit electron energy
dN_n/dE	Neutron flux per unit energy
$N_p(E)$	Total recoil protons per unit energy ($A\ dN_p/dE$)
$N_p(P)$	Total recoil protons per unit electron energy ($A\ dN_p/dP$)
$N_n(E)$	Total neutrons per unit energy ($A\ dN_p/dP$)
PSD	Pulse shape discrimination

UNCLASSIFIED

A NEUTRON SPECTROMETER USING ORGANIC SCINTILLATORS

D.W. Jones* and M.E. Toms

INTRODUCTION

In the past decade interest has increased in the use of organic scintillation detectors for neutron spectroscopy. Historically these scintillators were of little more than academic interest because of the difficulty involved in analyzing pulse-height spectra obtained from these detectors and because of their inherent sensitivity to gamma rays. More recently, methods have been developed to distinguish the pulses which are induced by neutrons from those induced by gamma rays, and to derive the energy spectrum of the neutrons incident upon the detector from the measured pulse-height distribution. The recent interest is due in part to these developments and in part to the availability of small computers which are needed for data analysis.

The object of an extensive program at NRL during the years from 1966 to 1969 has been to develop a practical neutron spectrometer using organic scintillators. The spectrometer developed at NRL consists of (a) a scintillation counter with an organic crystal as the fast-neutron detector, (b) a circuit for analyzing the shape of the current pulse from the scintillation counter to identify the particle which induced the scintillation, (c) a pulse-height analyzer and associated electronics for collecting the pulse-height data and (d) a computer program for analyzing the pulse-height data to extract the energy spectrum of the neutrons incident upon the face of the detector.

In the development of this spectrometer the optimum electronic system necessary for collecting data was studied in detail, and a new electronic circuit for analyzing the shape of the current pulse from the scintillation counter was developed. The interaction of neutrons with the scintillator was also studied in detail to obtain a nearly optimum method of pulse-height analysis. The neutron spectrometer developed at NRL has been used to measure both monoenergetic neutron spectra and continuous neutron spectra. In this report, a detailed explanation will be given of the electronic systems of the spectrometer and the analysis of the experimental pulse-height data to obtain the energy spectrum of the neutrons incident upon the detector. Examples will also be presented of the application of this spectrometer to the measurement of both continuous and discrete neutron energy spectra.

The primary purpose of this development was to provide a neutron spectrometer for photonuclear spectroscopy. During the course of this development the spectrometer has been applied to (a) measurement of the energy spectrum of monoenergetic neutrons produced by $D(d,n)$, $T(p,n)$, and $T(d,n)$ reactions; (b) measurement of the energy spectra of neutrons from the radioactive α-beryllium sources: *PuBe*, *AmBe*, and *PoBe*; (c) measurement of neutron elastic and inelastic cross sections; (d) measurement of the energy spectrum

*Present address: Memphis State University, Memphis, Tennessee.

of neutrons from the photonuclear reaction produced by 28-MeV bremsstrahlung on oxygen-16; and (e) detection of fission neutrons from uranium and plutonium isotopes for a Safeguards application. Most of these applications will be discussed in this report. Other potential fields of use include health physics, nuclear bomb tests, and any other need involving the measurement of fast neutrons.

The authors of this report acknowledge the use of the NRL Van de Graaff facilities for taking data and the advice of Dr. P. Malmberg and Dr. T. May. The advice of Dr. W.L. Bendel in the early stages of the computer programming is appreciated. Also the encouragement and advice of Dr. T.F. Godlove throughout the course of the development of this spectrometer are appreciated.

1. GENERAL DESCRIPTION OF NEUTRON SPECTROMETER

1.1 Block Diagram of Neutron Spectrometer

A block diagram of the neutron spectrometer developed at NRL is shown in Fig. 1.1. The scintillation counter consists of an organic scintillation detector, either stilbene or NE 213, mounted on a photomultiplier capable of high current output. Two pulses are taken from the photomultiplier: one from the anode and one from the 11th dynode. The pulse from the 11th dynode is integrated in a preamplifier to obtain an output voltage with an amplitude proportional to the total charge contributed by the scintillation to the charge pulse in the multiplier. This pulse is then shaped and increased by a linear amplifier to obtain a voltage pulse with an amplitude and shape compatible with the input to a 1024-channel pulse-height analyzer.

Because the detector is sensitive to both neutrons and gamma rays, it was necessary to develop a pulse-shape discrimination (PSD) circuit which analyzes the shape of the current pulse from the photomultiplier anode to determine the identity of the particle which induced the scintillation in the detector. The current pulse from the photomultiplier develops a voltage pulse at the input to this circuit across the terminating resistor of a length of coaxial

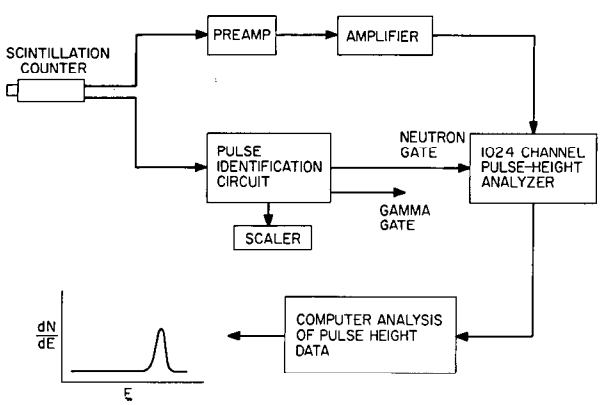

Fig. 1.1—Block diagram of neutron spectrometer

UNCLASSIFIED

cable. For the electronic analysis of the scintillation pulse the shape of the current pulse must be preserved at the input to this circuit; this purpose is achieved by properly terminating the 100-foot-long coaxial cables normally used in this spectrometer. If the PSD circuit determines that the scintillation in the detector was induced by a neutron, it provides a logic pulse to open the coincidence gate of the pulse-height analyzer. Therefore, only those pulses which were induced in the detector by neutrons are admitted to the pulse-height analyzer. A gamma gate is also provided by the PSD circuit if pulses induced in the detector are identified as due to gamma rays. This gating pulse may be used in a similar manner to simultaneously collect the pulse-height distribution due to gamma rays in another pulse-height analyzer. A third pulse permits the total number of pulses to be counted in a scaler or the counting rate to be measured in a count rate meter.

Because of the nature of the detector response, the pulse-height distribution stored in the analyzer does not bear a simple relationship to the energy spectrum of the neutrons incident upon the face of the detector. It was necessary, therefore, to develop a computer program to analyze the pulse-height distribution. The computer program developed at NRL derives the energy spectrum of the incident neutrons by first converting the pulse-height data to the energy spectrum of recoil protons and then calculating the neutron energy spectrum by differentiating the recoil proton spectrum. In Chapter 2 is a discussion of pulse-height data from recoil protons described in terms of an ideal proton spectrum with perturbations. Data analysis and the FORTRAN computer program are given in Chapter 3.

In the following sections, the details related to the construction of the scintillation counter will be discussed. Since the equipment used to collect the pulse-height data is commercially available, only those principles important to the selection of this equipment will be outlined. The details of the PSD circuit developed at NRL will be given in Chapter 5.

1.2 Scintillation Counter

A cross-sectional diagram of the scintillation counter is shown in Fig. 1.2. As indicated by this diagram, the scintillation counter consists of (a) a scintillation crystal, (b) a photomultiplier with electrostatic and magnetic shielding, (c) a high-voltage divider and the base for the photomultiplier tube, and (d) an aluminum case. An RCA-6810A photomultiplier was selected because the photocathode has high quantum efficiency and its response matches the emission spectrum from organic scintillators. This tube is capable of a high current output, thus eliminating the need for an amplifier preceding the PSD circuit. The cathode is operated at negative potential (nominally at 2000 V), and the anode is at ground potential to permit a signal to be taken directly from the anode without the need for a large coupling capacitor. A charge pulse is taken from the 11th dynode to provide a linear signal to the preamplifier.

To insure linearity over a large signal range the voltage divider, shown in Fig. 1.3 is used. This divider distributes a larger fraction of the anode-cathode voltage over the last few dynodes than dividers designed for high gain service. For proper operation of the PSD circuit it is necessary that both the total charge output of the photomultiplier be proportional to the total light output of the scintillator and the peak current output from the photomultiplier be proportional to the peak light output of the scintillator. The linearity of this

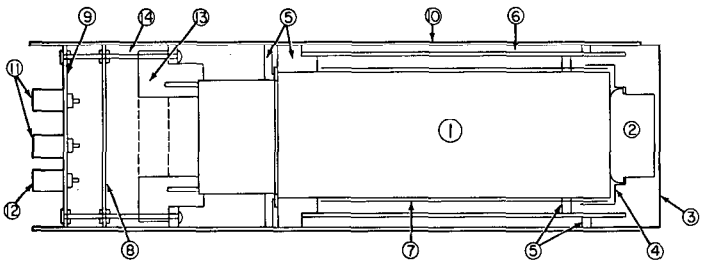

Fig. 1.2—Cross section of scintillation counter assembly:
1. RCA 6810A photomultiplier
2. Stilbene detector
3. Front-end cap (0.020-in. Al)
4. Holder for detector (0.020-in. Al)
5. Teflon spacers
6. Magnetic shield
7. Electrostatic shield
8. Divider string for PM
9. Back-end plate (0.060-in. Al)
10. Outside case (0.060-in. Al)
11. Output connectors
12. High-voltage input
13. PM base socket
14. Spacing screws.

peak current, up to 300 mA, is insured by having each dynode bypassed to ground through a capacitor large enough to reduce the signal voltage at that dynode to less than 1% of the voltage between that dynode and the adjacent ones. With this divider the current output of the photomultiplier is proportional to the light output of the scintillator up to a peak output current of 0.5 A.

Because of the negative potential applied to the cathode, both the electrostatic and magnetic shields must be maintained at high voltage. Insulation from the outside case is provided by Teflon spacers. The entire assembly is contained within a thin-walled aluminum tube with light-tight end caps. To reduce the neutron interactions with the scintillation-counter hardware, the thickness of the front end cap was reduced to 0.020 inch and the wall thickness of the tube to 0.060 inch.

The gain of the photomultiplier is largely dependent upon the voltage impressed between the anode and the cathode of the photomultiplier with the fractional gain dG/G approximately equal to $N\,dV/V$, where $N \approx 10$ for a 14-stage tube. As will be pointed out in Chapter 4, an overall system stability of ±1% is required when it is desired to define the energy of the neutrons incident upon the detector to within 0.1 MeV. Power supplies stable to within ±0.01% over the range of operating conditions are normally selected for this purpose.

UNCLASSIFIED

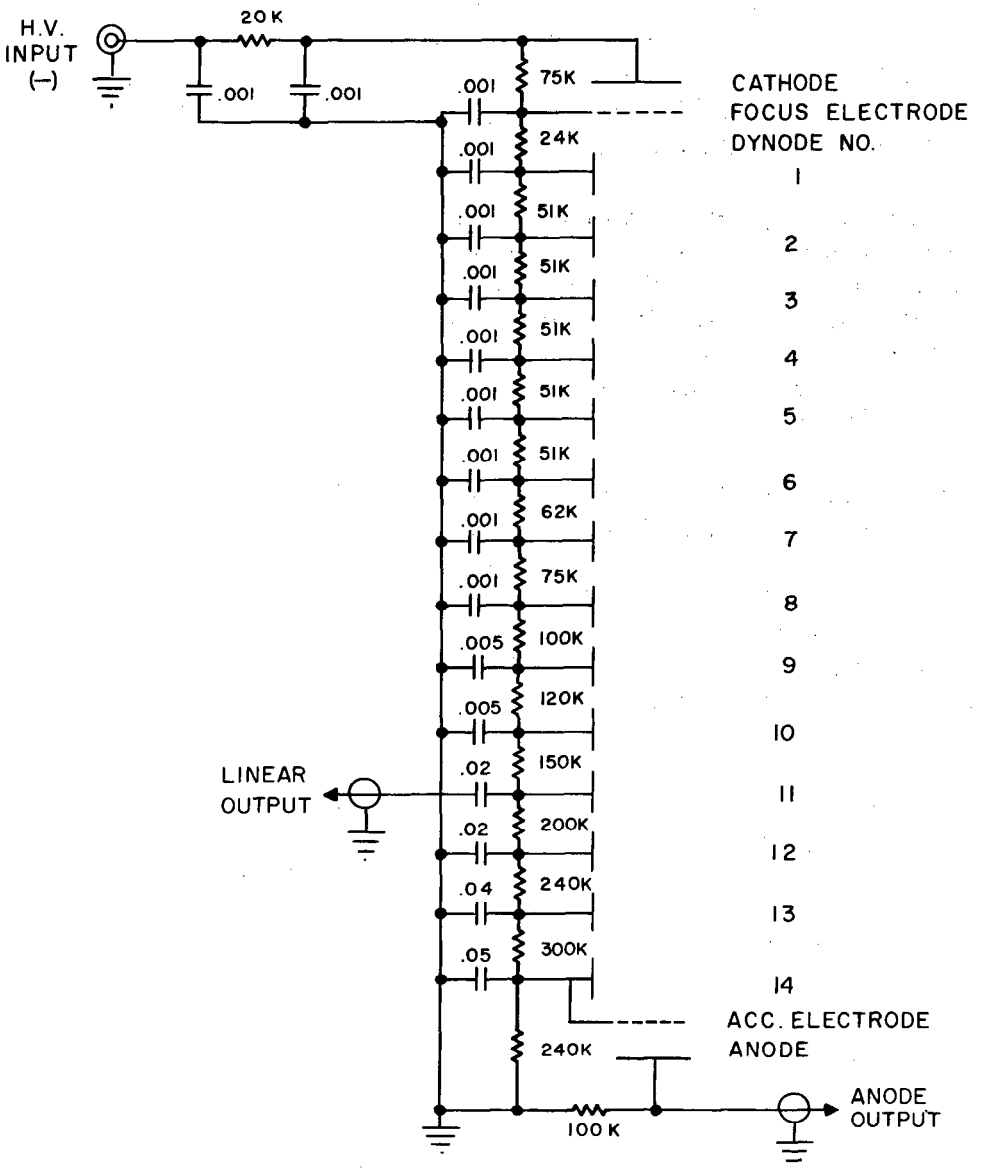

Fig. 1.3—High-voltage divider string for RCA 6810A. All resistors are rated at 1/2 watt and 5%. All capacitors are listed in microfarads. The ratings for the capacitors are: 3 kV for 0.001 μF; 2 kV for 0.005 μF and 0.02 μF; and 1 kV for 0.04 μF and 0.05 μF.

1.3 Pulse Amplifiers and Pulse-Height Analyzer

As illustrated in Fig. 1.1, the system used to collect a pulse-height distribution from the scintillation counter consists of (a) a preamplifier for integrating the charge pulse from the photomultiplier to obtain a voltage pulse proportional to the total charge pulse, (b) a linear amplifier for shaping and amplifying the voltage pulse to a range compatible with the input to the pulse-height analyzer, and (c) a pulse-height analyzer to collect the pulse-height data.

The output of the integrating preamplifier is determined by the magnitude of the charge delivered from the photomultiplier and is independent of the pulse shape only if the integrating time constant of the preamplifier is much larger than the decay time of the pulse from the photomultiplier. If the decay of the scintillation pulse is approximated by a series of exponentials, the decay time of the longest large component is about 300 nsec. Therefore, the integrating time constant of the preamplifier should exceed 10 μsec.

Both charge-sensitive preamplifiers and RC-integrating networks with emitter followers have been used successfully in this spectrometer. Either type is normally located near the photomultiplier, and its output is driven through a long cable to a remote linear amplifier. Because of electromagnetic pickup, it is often necessary to operate both amplifiers remotely from the scintillation counter. In this case, the current pulse from the scintillation counter may be converted to a voltage pulse developed across a cable termination and then integrated in an operational amplifier.

The primary purpose of the linear amplifier is to shape the preamplifier output so that a high counting rate may be obtained. For this purpose a double-delay-line amplifier is used in this spectrometer. The voltage gain serves only to convert the amplitude of the output from the preamplifier to a level compatible with the input of the pulse-height analyzer, while the double-delay-line differentiation reduces the effective width of the pulse to about 2 μsec. Although a shorter clipping time constant would permit higher counting rates, less than 2 μsec should not be used since the integrated charge pulse due to recoil protons does not reach its final amplitude until about 2 μsec after its appearance.

As will be discussed in Chapter 2, the sensitivity of the detector to both neutrons and gamma rays provides a unique method of calibrating the energy response of the detector. It is found that this calibration depends upon the characteristics of the detector rather than the electronics only if the current pulse of the scintillator is integrated with a time constant greater than 10 μsec and the clipping time constant of the linear amplifier is set to no less than 2 μsec.

The PSD circuit requires 1 μsec to analyze the current pulse from the photomultiplier to identify the particle which induced the pulse. Therefore, a delay of 1 μsec is required between the linear amplifier and the pulse-height analyzer. Often this delay may be obtained from the delayed output of a linear amplifier. The length of the delay varies with the type of pulse-height analyzer used.

1.4. Summary and Comment

In this chapter the basic features of the NRL neutron spectrometer have been described. The spectrometer is designed such that the scintillation counter can be operated remotely from the PSD circuit and the electronics used to collect pulse-height data. The upper limit of the energy range of the spectrometer is limited by the linearity of the photomultiplier while the lower limit of the energy range is established by the neutron-gamma discrimination ratio of the PSD circuit. Within these limits an operating range of 2 to 15 MeV neutron energy has been achieved. Within this range, the resolution of the spectrometer varies from 12.5% at 4.0 MeV to 6.5% at 8 MeV. The overall resolution of the spectrometer is limited

UNCLASSIFIED

primarily by the light conversion efficiency of the photocathode of the photomultiplier. Examples of measurements which exhibit this resolution are given in Chapter 4.

2. PULSE-HEIGHT DATA FROM RECOIL PROTONS

2.1. Introduction

Although neutrons interact with the hydrogen and carbon nuclei of organic scintillators by several different mechanisms, the detection of neutrons by an organic scintillator depends primarily upon elastic scattering collisions between neutrons and protons. From the scattering collisions a continuous distribution of recoil protons is obtained. These protons range in energy from zero up to the energy of the neutrons which produced them. As will be explained in this chapter, the energy-response function of the scintillator is nonlinear; therefore, the pulse-height distribution obtained from the scintillation counter will not be directly proportional to the energy spectrum of the recoiling protons. When the response function is determined, the pulse-height distribution can be converted to the recoil-proton energy spectrum, and a differentiation process can then yield the energy spectrum of the incident neutrons. This method is applicable both when the incident-neutron energy spectrum is monoenergetic and when it is continuous.

Other reactions of neutrons with the atoms of the detector serve to produce scintillations which may be considered as perturbations to the recoil-proton energy spectrum. Some of these reactions are (a) second scattering of the neutrons from hydrogen nuclei; (b) loss of recoiling protons through the end of the detector; and (c) elastic scattering, inelastic scattering, and other reactions with carbon atoms of the detector. The effect of each of these perturbations will be discussed in this chapter.

Gamma rays interact with the scintillator primarily by the Compton scattering process. As a result of these scattering collisions, recoiling electrons are produced which range in energy from zero up to a maximum energy called the Compton edge. The response of the scintillator to these recoil electrons is linear. This linear response provides a method by which the energy scale of the pulse-height analyzer can be calibrated before each experiment with gamma-ray sources provided that the electron and proton energies for equal response are known. This relation between the electron and proton energies for equal response and the method of calibration will be discussed in detail in this chapter.

2.2. Neutron-Proton Elastic Scattering

If we consider a beam of neutrons of energy E_o with a flux N_o incident upon a hydrogenous scintillator of area A and length L, it follows that the total number of protons N_p produced by single scattering collisions is given by

$$N_p = N_o A \epsilon(E_o, L), \tag{2-1}$$

where $\epsilon(E_o,L)$, the efficiency of the scintillator for producing recoil protons by single scattering collisions, is given (1) by

$$\epsilon(E_o,L) = n_h\sigma_h L(1 - e^{-aL})/aL = n_h\sigma_h L f(aL),$$

with (2-2)

$$a = n_h\sigma_h + n_c\sigma_c \text{ and } f(aL) = (1 - e^{-aL})/aL.$$

In this formula, n_h and n_c refer, respectively, to the numbers of hydrogen and carbon atoms per unit volume of the scintillator, σ_h is the neutron-proton scattering cross section, and σ_c is the total carbon interaction cross section for neutrons. This formula for the single-scattering efficiency neglects the possible production of recoil protons by neutrons once scattered by hydrogen or carbon.

As pointed out by Staub (2), it can be shown kinematically that the number of recoiling protons per unit energy in the laboratory system is proportional to the differential elastic-scattering cross section per unit solid angle in the center-of-mass (c.m.) system. If the neutron-proton scattering is considered to be isotropic in the c.m. system, the recoil proton distribution in the scintillator is given by the following formula which is derived in Appendix 1 (c.f. Eq. (A1-28)), for a monoenergetic incident beam:

$$N_p(E) = A\, dN_p/dE = [N_o A\epsilon(E_o,L)]/E_o. \tag{2-3}$$

If the spectrum of the incident neutrons is not monoenergetic but has a distribution dN_n/dE_o (neutrons per unit area per energy interval), then we must include the contribution to $N_p(E)$ of all neutrons above the energy E. Thus, in general

$$N_p(E) = \int_E^\infty [A\epsilon(E_o,L)/E_o](dN_n/dE_o)\, dE_o. \tag{2-4}$$

Differentiating both sides with respect to E and solving gives the energy spectrum of the incident neutrons in terms of the slope of the recoil-proton energy spectrum:

$$(dN_n/dE_o)_E = dN_n/dE = -(dN_p(E)/dE)[E/(A\epsilon(E,L))]. \tag{2-5}$$

Thus, from the energy of the recoiling protons, the energy spectrum of the incident neutrons can be obtained. However, an organic scintillator produces a pulse-height distribution which is nonlinear with respect to recoil-proton energies, and its output is subject to a number of perturbations which will be discussed.

2.3. Nonlinear Pulse-Height Response

Within the linear range of the photomultiplier, the total charge output of the scintillation counter is proportional to the total luminous output of the scintillation crystal. Details of the scintillator response have been outlined by Schwartz and Owen (1) and by Birks (3). As these authors point out, the luminous output of the scintillation crystal is, in general, not

UNCLASSIFIED

proportional to the energy lost in the scintillator by the charged particle. To describe this nonlinear response, the light output per unit energy loss in the crystal dS/dE can be related to the rate of energy loss by the charged particle dE/dx as it passes through the crystal (1) by

$$dS/dE = C[1 + kB(dE/dx)]^{-1}. \tag{2-6}$$

In this formula, the product of B, a constant, and dE/dx gives the specific density of ionized and excited molecules along the particle track. The quenching parameter k is characteristic of the scintillator for the particular ionizing particle, and C is a proportionality constant.

As Schwartz and Owen (1) observed, there are two limiting forms of Eq. (2-6). For light particles, such as electrons, dE/dx is small enough that the factor $kB(dE/dx)$ can be neglected and the integrated light output due to electrons S_e is proportional to their energy loss in the scintillator:

$$S_e = CE_e. \tag{2-7}$$

For heavier particles, such as protons, alpha particles, and ionized atoms, the factor $kB(dE/dx)$ cannot be neglected; hence, S is not directly proportional to the energy loss of the particle in the scintillator. For very heavy particles, such as fission fragments, dE/dx is sufficiently large that the term $kB(dE/dx)$ dominates the denominator of Eq. (2-6). When this occurs, the integrated light output S_p becomes proportional to the range $R(E)$ of the particle in the scintillator:

$$S_p = CR(E)/kB. \tag{2-8}$$

As a result of this nonlinearity, the pulse-height distribution collected in the pulse-height analyzer will not be proportional to the recoil-proton energy spectrum expressed as $N_p(E)$ in Eqs. (2-3) and (2-4). However, the pulse-height distribution can be converted to a recoil-proton energy spectrum if the response of the scintillator is known.

A convenient method of expressing the response of the scintillator is suggested by the linear relationship between the light output and the electron energy (c.f. Eq. (2-7)). The response can be expressed in terms of the electron and proton energies for equal total light output of the scintillator. When this is done, only an electron energy calibration of the pulse-height analyzer is needed to convert the pulse-height distribution to the recoil-proton energy spectrum. This electron energy calibration can be obtained from the Compton electrons produced in the scintillator by gamma rays as will be explained in this section. Thus, the need for a difficult proton energy calibration prior to each experiment is eliminated.

Some early data giving electron and proton response characteristics for several scintillators are summarized by Birks (3). The relation between the electron and proton energies for equal light output can probably be expressed best by a polynomial. However, the results of several experiments, listed in Appendix 2, demonstrate that the formula below can be used over the range from 2 to 15 MeV as a good approximation of the relation between the electron energy P and the proton energy E for equal light output.

$$P = \alpha E^{\beta}. \tag{2-9}$$

The constants α and β must be determined for each spectrometer; they depend primarily upon the type of scintillator used and its characteristics rather than the electronic system, provided that care is taken to insure that the pulse-height distribution collected in the pulse-height analyzer is proportional to the total light output of the scintillator (c.f. Section 1.3).

An example of the distortion produced by this nonlinear response is shown in Fig. 2.1, where the recoil-proton energy spectrum ($A\ dN_p/dE = N_p(E)$) was calculated from Eq. (2-3) and the recoil-proton pulse-height distribution ($A\ dN_p/dP = N_p(P)$) was calculated from Eq. (2-9). In this figure the recoil-proton pulse-height distribution is expressed in terms of the electron energy for equal charge response. The calculation was performed for monoenergetic neutrons of 8.0 MeV incident upon a stilbene scintillator 1 inch in diameter and 1 inch long. The constants α and β used are 0.150 and 1.5414 respectively with P and E expressed in MeV. As may be seen from this figure, the recoil-proton pulse-height distribution is distorted toward the lower energies and must be converted to a recoil-proton energy spectrum before a differentiation can yield the incident neutron spectrum.

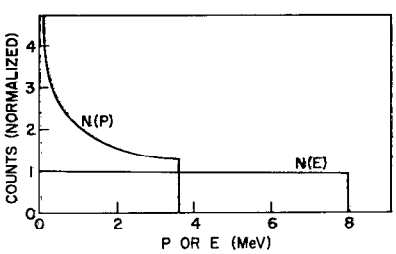

Fig. 2.1—Recoil-proton energy spectrum $N_p(E)$, here denoted as $N(E)$, produced by 8.0-MeV neutrons incident upon a stilbene crystal. The recoil-proton pulse-height distribution $N_p(P)$, here denoted as $N(P)$, is calculated from Eq. (2-9).

To obtain the response-function constants α and β of Eq. (2-9) for the neutron spectrometer discussed in Chapter 1, the electron and proton energies for equal charge response were measured in the following way. For the proton energy calibration, monoenergetic neutrons were obtained from $D(d,n)He^3$ and $T(p,n)He^3$ reactions using the facilities of the NRL 5-MV Van de Graaff. As an example, the pulse-height data obtained from monoenergetic 8.0-MeV neutrons are shown in Fig. 2.2. This distribution resembles the calculated distribution $N_p(P)$ shown in Fig. 2.1. For each of the pulse-height distributions needed for the proton energy calibration, the midpoint on the dropoff was used to determine the channel number corresponding to the maximum recoil-proton energy which equals the energy of the incident neutrons. The electron energy calibration of the pulse-height analyzer was obtained using monoenergetic gamma-ray sources. Gamma rays interact with the detector primarily by Compton scattering collisions with atomic electrons of the detector. The maximum energy of the recoiling electrons E_c commonly referred to as the Compton edge, bears a simple relationship to the energy of the gamma rays E_γ

$$E_c = E_\gamma/(1 + m_0c^2/2E_\gamma). \tag{2-10}$$

As an example, the pulse-height spectrum obtained from a monoenergetic source of gamma rays is shown in Fig. 2.3. The energy scale of the pulse-height analyzer is calibrated by assigning the energy of the Compton end point to the channel corresponding to the midpoint

UNCLASSIFIED

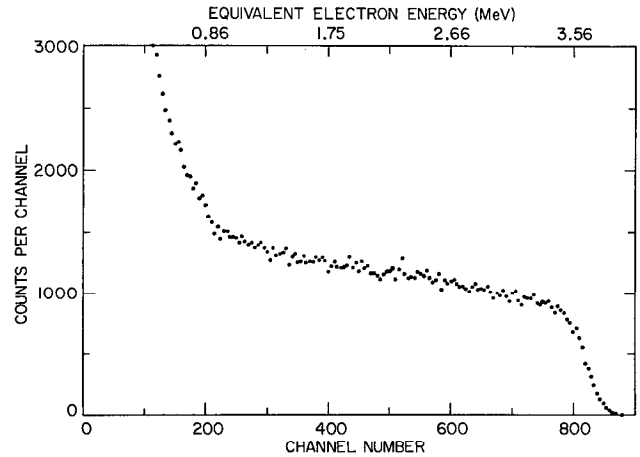

Fig. 2.2—Measured recoil-proton pulse-height distribution produced by 8.0-MeV neutrons incident upon a 1-inch-diameter-by-1-inch long stilbene crystal.

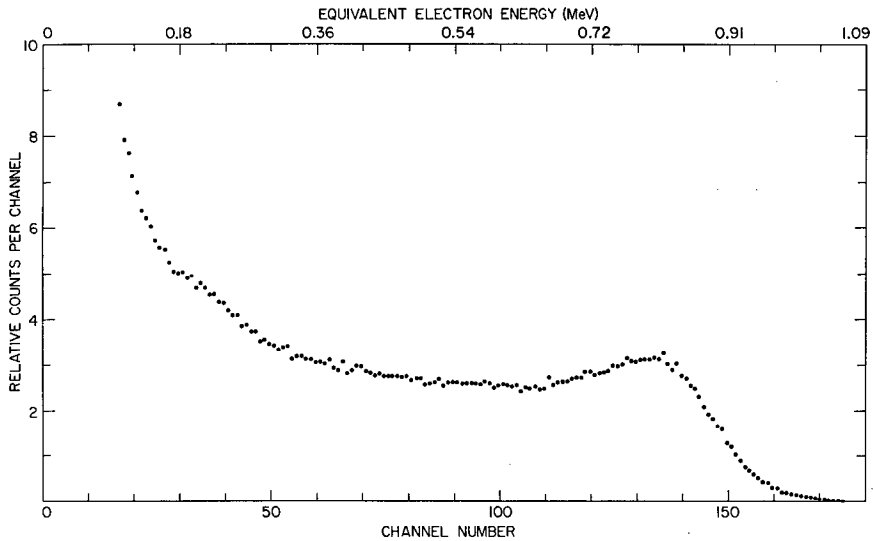

Fig. 2.3—Pulse-height spectrum produced by recoiling Compton electrons produced by monoenergetic gamma rays from Zn^{65}.

of the dropoff in the Compton spectrum. By comparing the electron energy calibration obtained using a number of gamma-ray sources with the proton energy calibration, the electron and proton energies for equal charge response are determined. The results of this measurement are shown in Fig. 2.4. From a straight line fitted to these data points, the constants α and β were found to be 0.150 and 1.5414, respectively. The response curves determined by Wasson (4) for alpha particles and recoiling C^{12} nuclei are also shown on this graph. Calibrations obtained by various experimenters are given in Appendix 2. The variation in slope and intercept of these calibrations is likely due to differences in values of the clipping time constants described in Section 1.3.

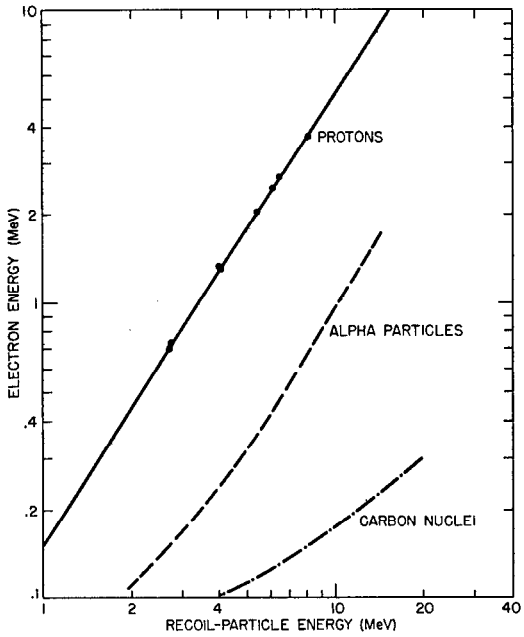

Fig. 2.4—Recoil-particle energy vs electron energy for equal charge response of a stilbene scintillation spectrometer. The points represent NRL data; the curves for alpha particles and carbon nuclei are from Ref. 4.

2.4. Perturbations of the Ideal Recoil-Proton Spectrum

In addition to the nonlinear response of the detector described in the preceding section, several perturbations to the detector response are introduced by the finite size of the detector, second scattering of neutrons by hydrogen, and elastic or inelastic scattering by carbon prior to scattering by hydrogen. These perturbations have been discussed by Schwartz and Owen (1) and by Broek and Anderson (5) for stilbene scintillators and by Batchelor et al. (6) for NE 213 detectors. The effect of these perturbations may be considered as producing distortions to the recoil-proton energy spectrum $N_p(E)$. These effects are discussed below and will be illustrated as distortions of a recoil-proton spectrum produced by a beam of monoenergetic neutrons of 8.0 MeV in a crystal 1 inch long and 1 inch in diameter.

2.4(a) Second Scattering of Neutrons

Because the efficiency for neutron-proton scattering increases with decreasing neutron energy, there is a high probability that a neutron, once scattered from a hydrogen nucleus, will collide with a second proton before escaping from the crystal. Consideration of the velocity of the neutron (1.5 nsec/cm for a 1-MeV neutron), along with the dimensions of commonly used scintillators, indicates that the pulses due to both protons will be separated by little more than a nanosecond. Since the decay time of the scintillation pulse is several nanoseconds, the light from both pulses will add and only one pulse will appear at the output of the photomultiplier. Therefore, the effect of a second scattering event is to remove a proton from the ideal recoil-proton energy spectrum $N_p(E)$ given by Eq. (2-3) and replace it by one whose energy is the sum of the one removed and the energy of the proton recoiling from the second collision. The neutron recoiling from the first collision in which a proton of energy E is produced has an energy $E_o - E$. Protons scattered by collisions with these

UNCLASSIFIED

neutrons will have an energy distribution ranging from zero up to $E_o - E$; therefore, the energy of the sum pulse will range from E to E_o. This summation in effect removes protons from the recoil spectrum at E and redistributes them from E to E_o. For simplicity, the proton energies are assumed to add although the scintillation response is nonlinear.

As shown in Appendix 1, the energy distribution of neutrons scattered from hydrogen dN_n/dE is identical in magnitude and shape to the recoil-proton energy distribution dN_p/dE. Therefore, the number of neutrons of energy $E_o - E$ which participate in a second scattering event is given by $N_p(E)\epsilon(E_o - E,L')$, where $\epsilon(E_o - E,L')$ is the efficiency of the detector for neutron-proton scattering for neutrons of energy $E_o - E$ produced inside the detector. The ideal recoil-proton energy spectrum $N_p(E)$ distorted by the second scattering of incident neutrons may be described as

$$N'_p(E) = N_p(E) - N_p(E)\epsilon(E_o - E,L') + \int_0^E [N_n(E)\epsilon(E_o - E,L')/(E_o - E)]\, d(E_o - E). \tag{2-11}$$

In this formula $N'_p(E)$ represents the distorted spectrum, and the second term represents those recoil protons removed from $N_p(E)$ at E per energy interval. The third term represents the number of protons added to the distribution at E after removal from the lower energy range by a second scattering event as explained above. This term is based on the assumption that the scintillation outputs due to the two protons add linearly. If it is assumed that the efficiency of the scintillator can be approximated by a function of the form KE^{-m} where $K = K(L')$ and $m \approx 0.5$, it is possible to perform the integration and thus derive from Eq. (2-11) an expression given by Schwartz, Owen, and Ames (7) (c.f. Appendix 3):

$$N'_p(E) = N_p(E) \left\{1 + K[(m^{-1} - 1)(E_o - E)^{-m} - m^{-1}E_o{}^{-m}]\right\}. \tag{2-12}$$

Using Eq. (2-11), the distorted recoil spectrum $N'_p(E)$ of protons resulting from 8.0-MeV neutrons has been calculated and is shown in Fig. 2.7a. As can be observed from this diagram, the effect of second scattering is to remove protons from the lower energy range and redistribute them in the upper energy range.

2.4(b) Loss of Recoil Protons

The range of a recoiling proton varies from approximately 0.02 mm at 1 MeV to 1 mm at 10 MeV. Therefore, a fraction of the recoil protons will escape the detector before losing all their energy. To calculate the effect of the loss of these protons from the crystal upon the ideal recoil-proton energy spectrum $N_p(E)$, we consider the protons lost through the end of the crystal and the protons lost through the sides separately. The geometry for the loss of protons through the end of the crystal is given in Fig. 2.5. The number of protons produced in the slab of thickness dx at a distance Z from the end of the crystal is given by $N_oAe^{-ax}n_h\sigma_h\, dx$, and their energy is determined by the angle of recoil $E = E_o \cos^2\theta$. The recoiling proton loses all its energy in the crystal only if the range traversed r is equal to the range $R(E)$ of the proton in the crystal. Therefore, the minimum distance Z_1 from the back surface at which a proton of energy E may be produced and still lose all its energy is given by $Z_1 = R(E)\cos\theta = R(E)(E/E_o)^{1/2}$.

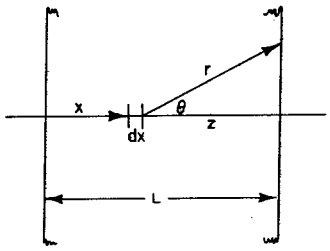

Fig. 2.5—Diagram for deriving the effect of proton loss through the end of a scintillator.

Protons of energy E produced in the region $Z < Z_1$ will never lose all their energy in the crystal and, therefore, will contribute to the recoil-proton energy spectrum at a lower energy. In the same way the numbers of protons at E may have contributions from protons produced in the crystal with energies greater than E. These protons will be produced in the region $Z_1 \leqslant Z \leqslant Z_2$, where Z_2 is the distance from the end of the crystal which will allow a proton of energy E_o recoiling in the forward direction to lose an amount of energy E in the crystal. The number of recoiling protons per unit energy $N_p(E')$ with $E' > E$ produced in slabs dx between Z_1 and Z_2 is related to the number of recoil protons per unit energy loss in the crystal, $N_p(E)$, by $N_p(E) = N_p(E')(dE'/dE)$. Therefore, the ideal recoil-proton spectrum with its distortion produced by the loss of protons through the end of the crystal is given by

$$N'_p(E) = (1/E_o)[N_o A n_h \sigma_h(E_o)(L - Z_1) f(a, L - Z_1)] +$$

$$(1/E_o)[N_o A n_h \sigma_h(E_o)] \int_{L-Z_2}^{L-Z_1} e^{-ax} \, (\partial E'/\partial E) \, dx. \qquad (2\text{-}13)$$

If the range of a proton of energy E in the crystal is approximated by $R(E) = KE^2$, where K is a proportionality constant, and if it is assumed that the fraction of the energy lost in the crystal E/E' is equal to the fraction of the range traversed $r/R(E') = Z/\cos\theta \; R(E')$, then, as in Appendix 4, Eq. (2-13) can be reduced to another equation quoted by Schwartz, Owen, and Ames (7) in their Appendix IV:

$$N'_p(E) = N_p(E) \left\{ 1 + (R_o/L)[(2/5) - (7/5)(E/E_o)^{5/2}] \right\} \qquad (2\text{-}14)$$

Using this equation the recoil-proton spectrum distorted by the loss of protons through the end of the scintillation crystal has been calculated for incident 8.0-MeV neutrons and is shown in Fig. 2.7b. The total number of recorded protons is, of course, not affected by this distortion, but the energy distribution is increased at low energies and depressed at the higher energies. Equation (2-14) indicates that the distorted spectrum is depressed most at $E = E_o$ by the fraction R_o/L, but it equals the ideal spectrum $N_p(E)$ at $E/E_o = 0.6$ or for 8.0-MeV neutrons at 4.8 MeV.

In the same way that protons produced within a distance Z_1 of the end of the crystal do not lose all their energy inside the crystal, those protons produced within some distance S of the edge of the crystal will also not lose all their energy inside the crystal. With the aid of Fig. 2.6, it can be seen that the distance S is given by $R(E) \sin\theta$. The approximations mentioned above, are used in Appendix 4 to show that

UNCLASSIFIED

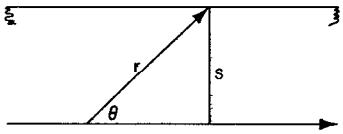

Fig. 2.6—Diagram for deriving the effect of proton loss through the sides of a cylindrical scintillator.

$$S = KE^2 [1 - (E/E_o)]^{1/2}. \tag{2-15}$$

The distance S can be written in terms of $R(E_o)$ as

$$S = R(E_o)(E/E_o)^2 \; [1 - (E/E_o)]^{1/2}.$$

Its maximum value occurs when $E = 0.8E_o$ and is zero when $E = E_o$. For incident neutrons of 8.0 MeV in energy, S is maximum for 6.4-MeV protons and has a value of 0.2862 $R(E_o)$. From the range of 8-MeV protons in stilbene given by Brodsky (8) as 79.65 mg/cm^2 and with the density being 1164 mg/cm^3, S_{max} for E_o = 8.0 MeV is 0.2 mm. If one considers a uniform flux on a crystal 1-inch in diameter, the ratio of the area of the ring of width $r - S_{max}$ to the total cross-sectional area is 0.03125 or 3.125%. The average value of S is approximately $S_{max}/2$ and as one half of the scattering occurs inwardly, the number of protons that leave the sides of the crystal are less than 1/4 of those scattered in a ring of width $r - S_{max}$. Hence, less than 0.8% of the recoil protons in a 1-inch-diameter crystal escape through the sides for an incident neutron energy of 8 MeV.

No analytical expression has been derived to describe this small effect, but the recoil-proton energy spectrum should not be affected at $E = E_o$ while being depressed most in the region $E = 0.8\,E_o$. At the lower energies the spectrum will be increased because of the contributions due to protons that escape the crystal. This effect is independent of the length of the crystal and depends only upon the radius and E_o.

2.4(c) Elastic Scattering from Carbon

The formula for the efficiency of the recoil proton detector, Eq. (2-2), is based upon the assumption that neutrons scattered from carbon atoms are lost from the scintillator. This, however, is true only to a first approximation since these neutrons can still participate in a proton scattering event. The energy of the neutrons scattered elastically from carbon nuclei is given by $E_n = E_o\ (0.858 + 0.142 \cos \alpha)$, where α is the angle of scattering in the c.m. system. Therefore, the energy of the neutrons range from $0.716E_o$ to E_o. As discussed in Appendix 1, the energy spectrum of the scattered neutrons in the laboratory system is determined by their angular distribution in the c.m. system. An examination of the differential scattering cross sections in this system indicates that neutrons with energies greater than 5.0 MeV are scattered primarily in the forward direction (8,9).

As shown by Eq. (A1-29), the energy spectrum of neutrons scattered elastically from carbon atoms is given by

$$(dN_n/dE)_c = [2\pi N_o n_c \sigma_c(E_n,E_o) L f(aL)]\,/0.142E_o. \tag{2-16}$$

These neutrons produce a recoil-proton energy spectrum in a scintillator of area A, expressed in integral form as

$$N_{pc}(E) = \int_{o}^{E_o} A(1/E_n)[n_h \sigma_h(E_n) L' f(aL')]\,(dN_n/dE)_c dE_n. \tag{2-17}$$

In these formulas, E_n represents the energy of the scattered neutrons and L' represents the effective path length for these neutrons inside the scintillator. The differential-elastic-scattering cross section is represented by $\sigma_c(E_n,E_o)$. The recoil-proton energy spectrum produced by these neutrons is flat from zero up to $0.72E_o$ and then decreases to zero at $E = E_o$. Therefore, the neutron-energy spectrum calculated from the distorted recoil-proton spectrum will show two broad groups between $0.72E_o$ and E_o. The variation in amplitude within this energy range reflects the angular distribution in the c.m. system of the neutrons scattered from carbon nuclei. Because of the peaks in the elastic scattering cross section, the magnitude of this effect will vary markedly with the energy of the incident neutrons. The effective length L' may also be a function of energy.

To demonstrate the effect of this scattering, the ideal spectrum with this distortion was calculated for 8.0-MeV neutrons and is shown in Fig. 2.7c. For this calculation, the differential scattering cross section in the c.m. system was taken from values tabulated by Garber et al (9). The effective length of the crystal L' was arbitrarily selected as $L/2$.

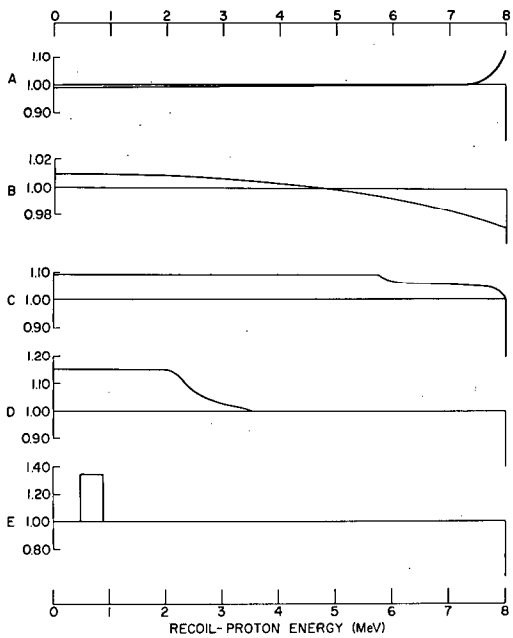

Fig. 2.7—Perturbations to the ideal recoil-proton energy spectrum for 8-MeV neutrons produced in a 1-inch-diameter-by-1-inch long stilbene crystal by (a) escape of protons through the end of the scintillator, (b) neutrons which have two scattering collisions with protons, (c) neutrons which scatter elastically from carbon before producing a recoil proton, (d) neutrons which scatter inelastically from the 4.43-MeV level of C^{12} before producing a recoil proton, (e) alpha particles produced by the $C^{12}(n,\alpha_o)Be^9$ reaction (scintillation pulses in terms of equivalent proton energy). Note changes in the scales of the ordinates.

2.4(d) Inelastic Scattering from Carbon

A fraction of the incident neutron beam will be scattered inelastically from one of the excited levels of carbon. In the calculation of the efficiency of the scintillator using Eq. (2-2), it is assumed that these inelastically scattered neutrons are lost from the scintillator,

UNCLASSIFIED

but some of them will also participate in elastic scattering collisions with protons in the scintillator. These inelastically scattered neutrons produce a perturbation in the recoil-proton energy spectrum given by

$$N_{pc*}(E) = \int_o^{E_o} A(1/E_n)[n_h \sigma_h(E_n) L' f(aL')](dN_n/dE)_{c*}\, dE_n \tag{2-18}$$

In this formula, $(dN_n/dE)_{c*}$ represents the energy distribution of the neutrons scattered inelastically from carbon (c.f. Eq. (A1-30)), and L' again represents an effective path length in the crystal for the scattered neutrons. Since the energy of a scattered neutron depends on the angle through which it is scattered, the energy spectrum of the scattered neutrons depends on the differential inelastic scattering cross section in the c.m. system. In the case of 8.0-MeV neutrons scattered from the 4.43-MeV level of carbon, the energy of the scattered neutrons will vary from 2.05 to 3.50 MeV. Figure 2.7d shows the ideal recoil-proton spectrum with the distortion calculated with the assumption that inelastic scattering occurs only from the 4.43-MeV level of C^{12}. The neutron spectrum derived from the distorted recoil-proton spectrum will show a group of neutrons between 2.0 and 3.5 MeV as a result of the inelastically scattered neutrons. Above 8.0 MeV, scattering from the 7.65-MeV level is possible and the energy spectrum will become more complicated. Because of the high probability of producing recoil protons by the low-energy neutrons scattered inelastically from carbon, spectra produced by high-energy neutrons will contain an important distortion in the low-energy region from this effect.

2.4(e) Alpha-Producing Reactions

Alpha particles can be produced in an organic detector by two reactions, $C^{12}(n,\alpha)Be^9$ and $C^{12}(n,n')3\alpha$. The threshold of the first reaction is about 6.2 MeV and the cross-section peaks at 0.08 barns near 8 MeV (10). The Q value of this reaction is −5.7 MeV so that the energy of alpha particles produced by 8-MeV neutrons will be less than 2.3 MeV and for 14-MeV neutrons less than 8 MeV (c.f. Appendix 1, Eq. (A1-31)). Reference to Fig. 2.4 shows that alpha particles of energy less than 8 MeV produce pulses less than 3-MeV proton equivalent. Therefore, the energy spectrum of recoil protons for 14-MeV neutrons will not be distorted above 3 MeV by pulses due to alpha particles. The alpha particles will produce a peak in the lower energy region of the pulse-height distribution. The energy spectrum of the alpha-particles dN_α/dE is discussed in Appendix 1.

The energy of the recoiling Be^9 nuclei will also be imparted to the crystal simultaneously with the energy of the alpha particles. Therefore, the light output of the scintillator will be the sum of the light produced in each scintillation. This effect, viewed as a distortion of the ideal proton distribution, is shown in Fig. 2.7e for 8-MeV incident neutrons. For simplicity, the energy distribution within the peak is assumed uniform. The effective threshold of the second alpha-producing reaction is 8 MeV, and the energy shared by the three alphas will produce a broad peak in the pulse-height distribution. This peak might be mistaken as being due to low-energy protons.

2.5 Interpretation of Perturbations

All the effects discussed in the preceding section will contribute to the distortion of the ideal recoil-proton energy distribution $N_p(E)$. To determine the magnitude of these effects on the ideal spectrum, the perturbations calculated in the preceding section were added to the ideal spectrum. The resulting distorted spectrum is shown in Fig. 2.8. For comparison, the recoil-proton spectrum calculated from the pulse-height distribution produced by 8.0-MeV neutrons incident on a 1-inch-by-1-inch stilbene crystal is shown in Fig. 2.8. The recoil-proton energy spectrum was obtained by correcting the pulse-height distribution for the nonlinear response of the detector as described in Section 2.3. For this comparison, the ideal spectrum was calculated for the same number of neutrons as were incident upon the detector. This flux was 1.925×10^6 neutrons/cm^2 from a measurement of monoenergetic neutrons which will be discussed in Chapter 4. As can be seen from this graph, the effect of the perturbations is to generate a significant group of recoil protons below 3 MeV, although not enough to explain the experimental data. Some disagreement between calculated and measured spectra is to be expected for a number of reasons. Since the effective length of the crystal for inelastically scattered neutrons must be approximated, the calculations cannot be precise; also no distortion was included for loss of protons through the sides of the crystal. This distortion would also serve to increase the number of low-energy protons and depress the spectrum around 6 MeV. The experimental data also include neutrons scattered from the scintillation counter assembly. The inelastically scattered neutrons from this source will further increase the recoil-proton spectrum at low energies.

At present no reliable procedure has been developed which can be used to remove all the effects of these perturbations from the neutron spectrum as derived from a distorted recoil spectrum. For monoenergetic spectra it may be possible to identify the effect produced by each perturbation and to discount it in the interpretation of the data. However, continuous neutron energy spectra are not so easily interpreted. Broek and Anderson (5) have developed a correction factor which removes most of the effects of second scattering and the loss of protons through the end of the detector. Their expression will be discussed in the next chapter in the section on data analysis.

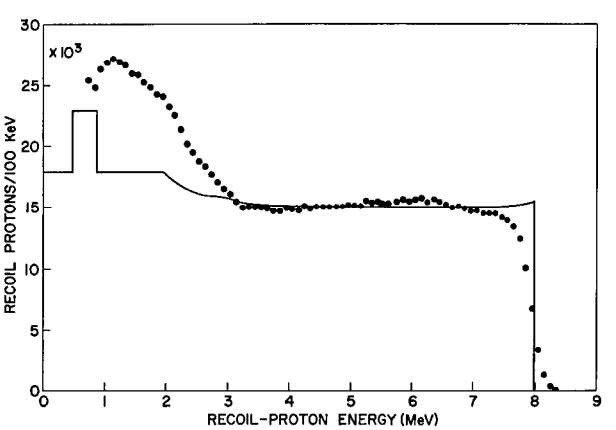

Fig. 2.8—Recoil-proton energy spectrum, shown as curve, calculated with sums of distortions for 8.0-MeV neutrons incident upon a 1-inch-by-1-inch stilbene crystal. Experimental data are shown as the dots. In each case the flux was 1.925×10^6 neutrons/cm^2.

UNCLASSIFIED

3. DATA ANALYSIS AND COMPUTER CODE

3.1. Data Analysis

In this chapter is described a method of analysis for converting pulse-height data, produced by recoil protons in a scintillation detector, to neutron spectra. This analysis is much simpler than the widely used matrix or Monte Carlo methods. It includes corrections for second scattering of neutrons by hydrogen and for loss of protons through the end of the detector. The computer code was originally developed for a small computer which had a 30-bit, 4096-word memory; hence, the code can be adapted for use with comparable computers, such as 16-bit minicomputers, small enough for field use. However, for the sake of clarity the program is presented here in FORTRAN IV compatible with a CDC 3800 computer.

In Chapter 2, the basic concepts concerning pulse-height data from a scintillator due to recoil protons have been discussed. Certain characteristics of the detector have been described as causing perturbations on the ideal recoil-proton energy spectrum. To obtain a recoil-proton energy spectrum from which to derive a neutron spectrum, the pulse-height distribution must be corrected for the nonlinear response of the detector. Since the scintillator was calibrated in terms of proton energy vs electron energy for equal pulse height, the response function expressed in Eq. (2-9) is used. For this spectrometer, it is

$$P = 0.150E^{1.5414} \tag{3-1}$$

where P is the electron energy and E is the proton energy. Values of P for 0.1-MeV energy intervals of E are listed in Appendix 5. Calibration of the pulse-height analyzer with gamma-ray sources relates the electron energy P of the Compton edge E_c defined in Eq. (2-10) to the channel number k by

$$P = a + bk. \tag{3-2}$$

For each pulse-height distribution the constants a and b are obtained from a least-squares fit to the gamma-ray calibration data. The computer program uses stored values of Eq. (3-1) together with Eq. (3-2) to relate channel numbers to proton energies. It then sums over channels to obtain protons per energy interval as here described. Let the channel number corresponding to the lower limit of a proton energy interval be designated k_s, and the one for the upper limit designated k_t. As these are generally noninteger, let $k_s = i_s + f_s$ and $k_t = i_t + f_t$ to separate the integer and fractional values for each limit number. By letting the numbers of counts per channel be designated N, the number of protons in an energy interval N_p is given by

$$N_p = (1 - f_s)N_{i_s+1} + N_{i_s+2} + \ldots\ldots + N_{i_t} + (f_t)N_{i_t+1}. \tag{3-3}$$

Equation (2-5) relates the neutron spectrum to the proton spectrum. With the shape-correction factor B included, the neutron flux dN_n/dE can be expressed as the product of a spectrum conversion function $\psi(E)$ with the negative of the slope of the proton spectrum

defined as $-q/\Delta E = dN_p(E)/dE$, at the center of the corresponding neutron energy interval ΔE:

$$dN_n/dE = \psi(E)(-q/\Delta E), \tag{3-4}$$

with $\psi(E) = E/A\epsilon_n B$. In the expression for $\psi(E)$, E is the neutron energy, A is the cross-sectional area of the detector, B is the shape-correction factor, and ϵ_n is the efficiency for neutron detection by means of recoil protons as expressed in Eq. (2-2). This expression contains neutron cross sections for hydrogen and carbon. For the latter, tabulated values of the total cross section (10), were used, and for the neutron-proton scattering cross section the formulation given by Schwartz, Owen, and Ames (7) as the sum of two terms was used. The first term is 1/4 of the singlet interaction while the second term is 3/4 of the triplet interaction. The expression in barns is

$$\sigma_h = 5.603\pi/(1 + 7.417E + 0.1105E^2) + 0.8652\pi/(1 + 0.2427E + 0.0028E^2) \tag{3-5}$$

with E expressed in MeV. The products of the number of atoms of hydrogen and carbon per cm^3 of stilbene with their respective cross sections, $n_h\sigma_h$ and $n_c\sigma_c$, are listed in columns 3 and 4 of Appendix 5. The values of neutron efficiency ϵ_n for three lengths of stilbene are listed in Appendix 6 and are graphed in Fig. 3.1. The deviations from a smooth curve are due to fluctuations in the carbon cross section. For short crystals, up to 1/2 inch, these fluctuations are negligible. As the graph indicates, the effect of the carbon cross section is increasingly pronounced with increasing length. To understand this, the expression for ϵ_n can be written as

$$\epsilon_n = (n_h\sigma_h/a)(1 - e^{-aL}), \tag{3-6}$$

which shows that the length dependence is only in the exponential term.

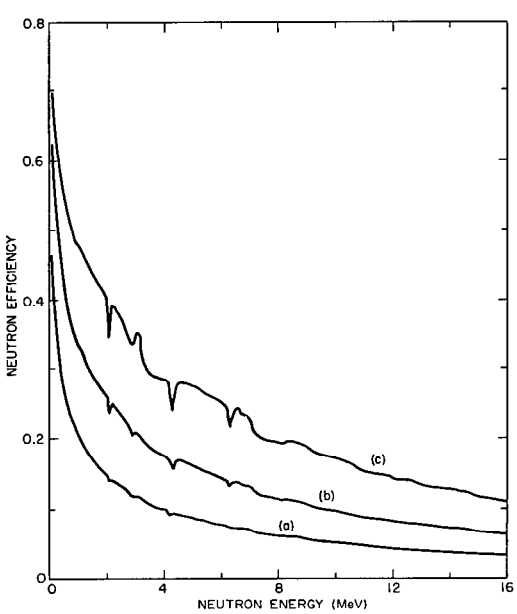

Fig. 3.1—Neutron efficiency ϵ_n given by Eq. (3-6) as a function of energy for stilbene crystals of lengths: (a) 1/2 inch, (b) 1 inch, and (c) 2 inches.

UNCLASSIFIED

The shape-correction factor B, given by Broek and Anderson (5), removes most of the effects of second scattering of neutrons by hydrogen and the loss of recoil protons through the end of the crystal. It may be written as

$$B = 1 - 0.780(R_m/L) + 0.090 n_h \sigma_h L + 0.077 n_h \sigma_h{}' r, \tag{3-7}$$

where $\sigma_h{}'$ is the value of σ_h at $0.068E$. In the second term, which corrects for the escape of protons through the end of the crystal, L must be in the same units as R_m, the range of a proton that receives the full neutron energy. In the third and fourth terms, which correct for second scattering, L and r, the radius, are expressed in centimeters. For stilbene, Brodsky (8) gives $R_m = 1.780(E - 0.119)^{1.815}$ mg/cm^2. The coefficients in the expression for B were obtained by Broek and Anderson by correcting at 90% of full pulse height the distortion caused by the end effect and by second scattering by hydrogen. The magnitude of the neutron peak derived from a pulse-height distribution produced by monoenergetic neutrons is corrected by this factor.

The spectrum conversion function $\psi(E)$ from Eq. (3-4) is tabulated in Appendix 6 for 1-inch-diameter crystals of lengths for which the neutron efficiencies are listed and also for a crystal 3/2-inches in diameter and 1 inch long. This crystal has a volume only slightly larger than that of the 1-by-2-inch crystal; hence, a comparison of the ψ-function values for these two crystals illustrates the dependence of $\psi(E)$ on the crystal shape.

To select an optimum method for calculating the slope of the recoil-proton energy spectrum, various formulations were used. Early calculations showed that it was possible to standardize on a neutron-energy bin width ΔE of 100 keV. It was found that resolution could be maintained and statistical accuracy improved by omitting, in the calculation of the slope, the numbers of protons in energy bins on each side of the neutron energy. If we let the numbers of protons in energy bins from the neutron energy be labeled P_1, P_2, P_3, and P_4 toward increasing energy and P_{-1}, P_{-2}, P_{-3}, and P_{-4} toward decreasing energy, five formulations for the slope and its uncertainties are

$$-q_2/\Delta E = (P_{-2} - P_2)/3\Delta E \qquad \delta_2 = (P_{-2} + P_2)^{1/2}/3\Delta E$$

$$-q_3/\Delta E = (P_{-3} - P_3)/5\Delta E \qquad \delta_3 = (P_{-3} + P_3)^{1/2}/5\Delta E$$

$$-q_4/\Delta E = (P_{-4} - P_4)/7\Delta E \qquad \delta_4 = (P_{-4} + P_4)^{1/2}/7\Delta E$$

$$-q_{23}/\Delta E = (P_{-3} + P_{-2} - P_2 - P_3)/8\Delta E \qquad \delta_{23} = (P_{-3} + P_{-2} + P_2 + P_3)^{1/2}/8\Delta E$$

$$-q_{34}/\Delta E = (P_{-4} + P_{-3} - P_3 - P_4)/12\Delta E \qquad \delta_{34} = (P_{-4} + P_{-3} + P_3 + P_4)^{1/2}/12\Delta E$$

Tests with actual data verified that for $-q_2/\Delta E$ the greater resolution is more than offset by greater statistical fluctuation. For $-q_3/\Delta E$ and $-q_4/\Delta E$ the resolution decreased while the statistical fluctuations also decreased. For $-q_{23}/\Delta E$ and $-q_{34}/\Delta E$ the resolutions were approximately equivalent to those for $-q_3/\Delta E$ and $-q_4/\Delta E$ respectively while the statistical fluctuations were significantly less. The formulation for $-q_{23}/\Delta E$ was chosen over that for $-q_{34}/\Delta E$ as the improved resolution was more important than a slight decrease in statistical uncertainties.

As discussed earlier, scintillation neutron spectrometers must incorporate a means of distinguishing between pulses due to neutrons and those due to gamma rays, either by time-of-flight separation or by pulse-shape discrimination. Even with PSD circuitry, there remains the problem of pile up of gamma-ray pulses. In some cases, such as detection of neutrons from photonuclear reactions, the detector must be shielded with lead to decrease the gamma flux. The efficiency of such detectors for gamma rays as well as for neutrons is important in choosing the length of the detector. A study (11) has been made of the efficiencies as a function of length for various energies and of the effect of size and shape upon the correction factor B and the spectrum-conversion function ψ. The graphs of gamma-ray and neutron efficiencies for stilbene are shown in Fig. 3.2.

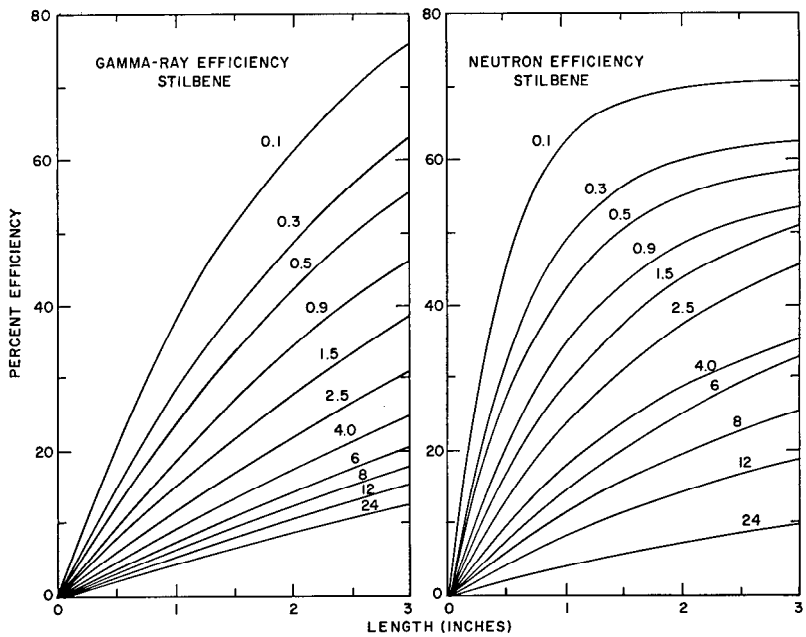

Fig. 3.2—Gamma-ray and neutron efficiencies for stilbene for energies from 0.1 to 24 MeV.

3.2. Computer Code

The FORTRAN code, listed in Appendix 7, processes, in 0.1-MeV intervals, pulse-height data from a 1024-channel analyzer to obtain neutron spectra up to 16 MeV. The 160 values for P, listed in Appendix 5, are designated PTAB. Likewise the 160 values of ψ, appropriate to the detector being used, are designated PSI. Another input is a control labeled KEY which designates the number of data sets (up to 9) which are to be combined. For each data set, DATA(I), a title card and values of A and B from the gamma-source calibration are required. Storage is provided for the proton energy spectrum PROT, the neutron spectrum SPEC, and its uncertainty, DEL. As seen in Appendix 8, the title, the calibration values, and the heading of the output table are printed. If KEY is greater than 1, a new output table is printed for each summing process.

UNCLASSIFIED

Calculations begin with the DO 50 statement. The calculation loop is set for a maximum of 159 cycles to correspond with the maximum neutron energy of 16.0 MeV. The values of P corresponding to the current E and $E + 0.1$ are obtained from the P table and used with A and B to find the lower and upper channel numbers, designated $C1$ and $C2$. If $C1$ is negative or zero, the loop recycles for a new $E = E + 0.1$. The number $C2$ is tested for being greater than 1024 and when this occurs the loop is terminated. When $C1$ is positive and $C2$ is less than 1024, the calculation continues by obtaining the sum of the protons for that energy bin. As $C1$ and $C2$ are generally noninteger, the sum is obtained as follows: (a) the integer part of $C1$, $L1$, is increased by one and designated $D1$ and the fraction $F1$, given by $D1 - C1$, multiplies the number of proton pulses in channel $D1$; (b) the integer part of $C2$, $D2$, plus one gives the channel number for the number of proton pulses to be multiplied by the fraction $F2 = C2 - D2$; (c) to the numbers found in steps (a) and (b) are added the number of proton pulses in the channels from $D1 + 1$ through $D2$. This sum of the protons in the energy interval E to $E + 0.1$ is stored as *PROT(J)* and in a working energy bin. The first value is stored in the bin labeled $PP1$, the second one in $PP2$, and the third and subsequent ones in $PP3$. The first three entries in the table (Appendix 8) give the lower limit of the proton energy, the lower channel number, and the numbers of protons in the 0.1-MeV energy bin. When fourth and subsequent protons sums are obtained, the values in the bins are shifted toward $PM3$ before the currently calculated value is placed in $PP3$. After the sixth sum is found, $PM3$ contains the first sum and the first neutron flux value can be obtained. The negative slope $-q$ is found as $(PM3 + PM2 - PP2 - PP3)/8$. It is designated *QNEG* in the program and is listed in the output table. The neutron flux value, designated *SPEC(K)*, is obtained by multiplying $-q$ by the value of ψ at the central energy E and dividing by ΔE (0.1 MeV in the program). The statistical uncertainty, designated *DEL(K)*, is obtained by substituting for $-q$ its uncertainty, i.e. $(PM3 + PM2 + PP2 + PP3)^{1/2}/8$. These two values are listed in the output table under NEUT and DEL. After the looping is completed, the last two values of E, the channel number, and the number of protons are printed. Sums of protons *PROT(J)* and neutrons *SPEC(K)* having energies in the ranges 4.0 to 6.9, 7.0 to 10.9, and 4.0 to 10.9 MeV are found and printed. Limits on these sums were chosen for a photonuclear experiment and can be modified easily to suit any experiment.

Besides the tabular output, provision is made for punching the neutron-flux values and their uncertainties on cards. The input CID is a card identifier of four characters. Eight values of neutrons are punched on a card with the CID and a card number and likewise for the uncertainties. This computer analysis together with a discussion of its advantages and limitations has been described elsewhere (12).

3.3 Programming for a Small Computer

Features concerning the original code for the data analysis of this chapter will be given only as a guide. Some suggestions are made for modifications to conform to the requirements of newer and faster small computers. The data analysis was first programmed for a Librascope General Precision computer which had a word length of 30 bits, LGP-30. It had a magnetic-drum memory consisting of 64 tracks and 64 words each or a total memory of 4096 words. Fixed-point, machine-language programming was used together with certain subroutines. The more standard word length of 16 or 18 bits in recent computers may make double-precision or floating-point arithmetic necessary so that, in general, double the number of words of memory should be sufficient.

For the LGP-30, a Program Input Routine (3 tracks), which interprets simplified machine-language programming, is used for reading in the program, subroutines, and tables. Subroutines used by the program were a Square-root Routine (1 track), Data Input (0.5 tracks), and a Data Output Routine (4.5 tracks) used for printing the output table. Two additional subroutines were stored on the drum, the Hexidecimal Print and Punch (5-tracks) used for making data output tapes and the Decimal Memory Print (4 tracks) used for diagnostic purposes. With one track assigned for storage for subroutines, a total of 19 tracks were kept constant for this data analysis. The 1024 items of pulse-height data occupied another 16 tracks. The P table and the ψ table needed 160 locations each for a total of 5 tracks. Storage needed for program-generated quantities amounted to 12.5 tracks (2.5 tracks each for the proton spectrum, the neutron data spectrum, its uncertainties, the neutron background spectrum and its uncertainties). The program itself including working storage fitted into 9.5 tracks. This left only two tracks not utilized.

Without the Decimal Memory Print and the separate storage for the background neutron spectrum and its uncertainties, there would have been 11 tracks not utilized. The separate locations for background and data were needed for the photoneutron experiment as will be explained in Section 4.3. Tapes of the data and background spectra made using the Hexidecimal Print and Punch permitted the spectra to be read back into the same locations for further processing by an additional program.

Programming in machine or assembly language rather than a compiler language saves memory space and time for execution; both features were important for the LGP-30 computer. Maximum use of looping, sense switches and subsections, such as a section for clearing 160 locations, was made in the LGP-30 program to minimize the program length. For newer, faster computers a section to calculate P might occupy less space than that needed for the P table.

The FORTRAN code, listed in Appendix 7, can be used as a guide for determining the various steps and looping processes needed for this type of data analysis. The individual small computer may have features that simplify certain procedures when machine-language programming is used. As an example, the process of separating the integer and fractional parts of the calculated channel numbers was easily accomplished using an extract order with an appropriate mask.

4. EXAMPLES OF DATA ANALYSIS

4.1. Monoenergetic Neutron Spectra

A good test of both the equipment and the method of analysis is performed when the energy spectrum of a monoenergetic beam of neutrons is measured. For this purpose a deuterium target was bombarded by deuterons accelerated to 4.754 MeV by the NRL Van de Graaff. The deuteron target was 40-keV thick so that a nearly monoenergetic beam of neutrons, 8.0 ± 0.025 MeV, was produced at zero degrees. The detector described in Chapter 1 was oriented such that the neutrons were incident normally upon the face of a cylindrical stilbene crystal 1 inch in diameter and 1 inch long.

UNCLASSIFIED

The pulse-height data, collected in 1024 channels, were analyzed by the method described in the preceding chapter. The derived neutron spectrum is shown in Fig. 4.1 where the fwhm of the peak, centered about 8 MeV, is 500 keV. This value indicates that, after taking out the effect of energy spread of the neutrons from the target, the overall resolution of the system was 430 keV at 8 MeV. The computer output for the analysis of these data is given in Appendix 9, where it can be seen that at channel 600, 100 keV of proton energy corresponds to 14 channels of pulse-height data. As the usefulness of this spectrometer depends upon the accuracy with which the energy scale is defined, the energy drift must be contained within a single 100-keV bin. This equipment provides the required stability of ±7 channels at channel 600 by having an overall drift of ±1%*.

The spectrum, produced by 8-MeV incident neutrons, was obtained by using the computer code previously described which included corrections for second scattering by hydrogen and for loss of protons through the end of the scintillator. As no corrections were made for the other perturbations discussed in Chapter 2, this computer analysis permits the observation of these effects, namely, the appearance of groups of neutrons in the spectrum between 6.0 and 7.5 MeV and between 2.0 and 3.5 MeV. In view of the discussion in Chapter 2, the first group immediately below the peak is considered to be due to neutrons elastically scattered with carbon before producing recoil protons. The energy range of the lower energy group is that which was predicted for inelastically scattered neutrons from the 4.43-MeV level of carbon. The magnitude of this group is 184,860 neutrons/100 microcoulombs compared with 1,849,000 neutrons/100 microcoulombs in the main peak at 8 MeV (the numbers for the lower energies were made symmetric with the high-energy tail). If the effective length for neutron-proton scattering after a scattering from carbon is taken to be $L/2$ and the average value of the scattered-neutron energy is used, the ratio of the inelastically scattered neutrons to the full-energy neutrons is calculated to be 0.06 compared with 0.10 from the measured peaks. The discrepancy between these ratios indicates that additional neutrons appear in the measured spectrum. These neutrons could be derived from additional inelastic scattering reactions with the material surrounding the scintillator which is composed primarily of aluminum. No attempt has been made to estimate the effect of these reactions.

An additional test of the method of analysis is obtained by comparing the number of neutrons in the peaks of the derived spectra with the number of neutrons incident on the crystal as calculated from the $H^2(d,n)He^3$ differential cross section at zero degrees and experimental parameters. The neutron flux at the detector position in units of neutrons/cm^2-μC is obtained from

$$F = 3.15 \times 10^5 Pk\sigma(d,n)(1/D^2), \qquad (\pm 10\%) \qquad (4\text{-}1)$$

where P is the pressure in atmospheres, k is the thickness of the gas target, and D is the distance from the center of the gas target to the face of the detector. For this test, the energy spectra of neutrons of 2.0, 4.0, 6.0, and 8.0 MeV were measured using a stilbene crystal 1 inch long and 1 inch in diameter. The neutron spectra derived from these measurements are shown in Fig. 4.2. Similar measurements were made using a 1/2-inch-by-1-inch crystal, and

*In Chapter 1 it was pointed out that an electronic stability of 0.01% was desirable to provide the required stability.

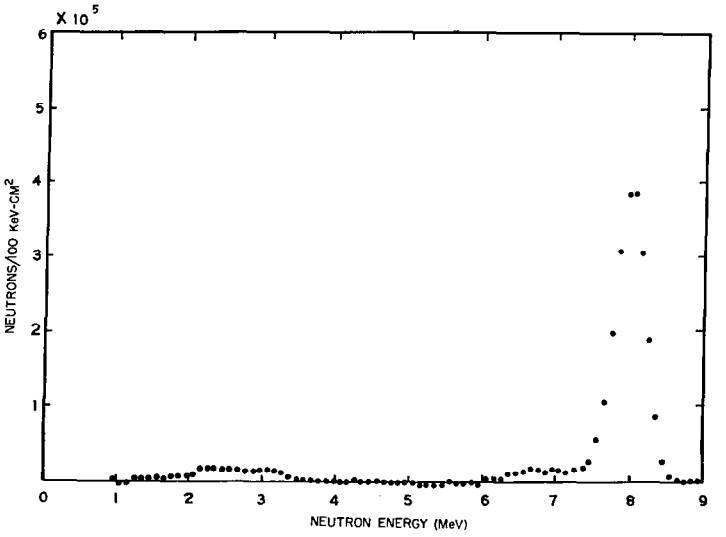

Fig. 4.1—Neutron spectrum derived from the pulse-height distribution produced by a flux of 1.925 X 10^6 neutrons/cm^2 of 8.0-MeV neutrons on a 1-inch-by-1-inch stilbene crystal. This spectrum was derived from the recoil-proton distribution shown in Fig. 2.8, and the computer output of the analyzed data is given in Appendix 9.

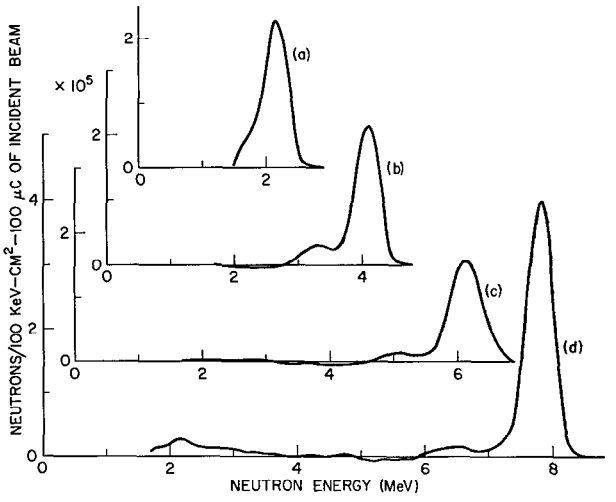

Fig. 4.2—Neutron spectra derived from data obtained with monoenergetic neutrons incident on a 1-inch-by-1-inch stilbene crystal. The spectra are for (a) 2-MeV neutrons, (b) 4-MeV neutrons, (c) 6-MeV neutrons, and (d) 8-MeV neutrons. Note: Spectrum d is not from the same data as that for Fig. 4.1.

the derived spectra are shown in Fig. 4.3. The measured values, based on the peak only (as the code compensates for loss of scattered neutrons), are compared with calculated values for both detectors in Table 4.1. Although the uncertainties in the measurements were not analyzed in detail, the discrepancies show that these uncertainties are about equal to the uncertainties in the calculations of the neutron flux.

UNCLASSIFIED

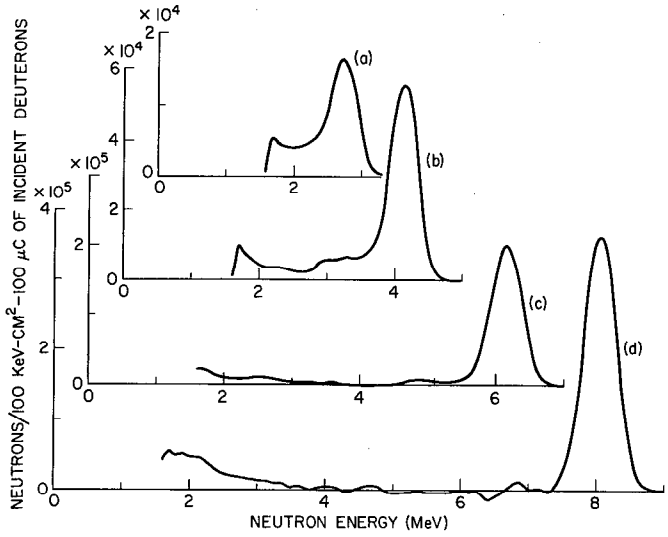

Fig. 4.3—Neutron spectra derived from data obtained with monoenergetic neutrons incident on a 1-inch-diameter and 1/2-inch-long stilbene crystal. The spectra are for (a) 2.7-MeV neutrons, (b) 4-MeV neutrons, (c) 6-MeV neutrons, and (d) 8-MeV neutrons.

Table 4-1
Comparison of Measured and Calculated Neutron Flux

Energy (MeV)	Resolution (keV)	Measured Flux	Calculated Flux	Discrepancy
1-inch-X-1-inch Stilbene				
8.0	478	19804	26760	−26%
6.0	624	10234	12770	−20%
4.0	480	9544	11194	−15%
2.0	500	9541	7774	+23%
1-inch-X-1/2-inch Stilbene				
8.0	568	21767	22530	− 4%
6.0	535	11360	13360	−15%
4.0	440	2586	3443	−25%
2.7	444	757	664	+14%

4.2. Energy Spectra of Neutrons from α-n Sources

The usefulness of this spectrometer for measuring continuous neutron spectra is illustrated by the results of measuring neutrons from a 1-curie *PuBe* source. For this measurement, a 1-inch-by-1-inch cylindrical stilbene detector was placed 30 cm from the neutron source for 2635 minutes. The computer analysis of the pulse-height data is given in

Appendix 8, and the measured spectrum is presented in Fig. 4.4. This spectrum has better resolution than published spectra measured with scintillation spectrometers and processed by other computer codes (c.f. Ref. 12).

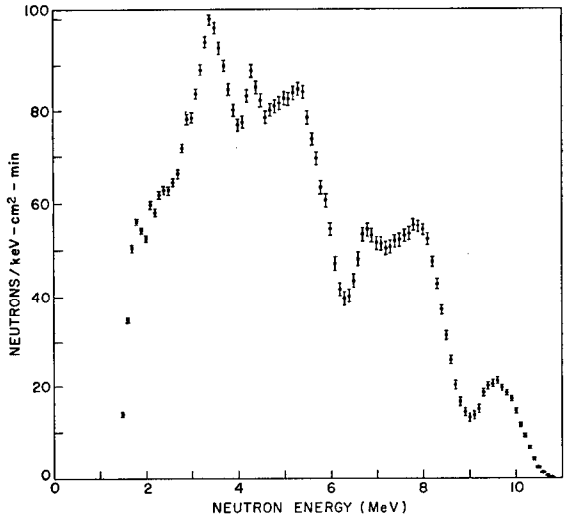

Fig. 4.4— Spectrum of neutrons from a *PuBe* source; the computer analysis of the data is given in Appendix 8.

Neutrons from a *PuBe* source are produced by the $Be^9(\gamma,n)C^{12}$ reaction. For an average alpha energy of 5.14 MeV from *Pu*, this reaction is such that neutrons emitted with energies of 6 MeV or greater leave C^{12} in its ground state, neutrons between 3.3 and 5.9 MeV in energy leave C^{12} in the 4.43-Mev excited state, and neutrons emitted with energies below 2.8 MeV leave C^{12} in the 7.66-MeV excited state. A theoretical calculation by Van der Zwan (13) and the measurement by Rubbino et al. (14), who used a different method of detection, are compared with the NRL measurement in Fig. 4.5. For this comparison, the theoretical calculation and the data of Rubbino et al. were normalized to the NRL measurement of ground state neutrons by normalizing the integral of their values above 6 MeV. As both experimental measurements below 6 MeV are lower than the magnitude predicted theoretically, the indication is that this theory predicts too much excitation of the 4.43-MeV state of C^{12}.

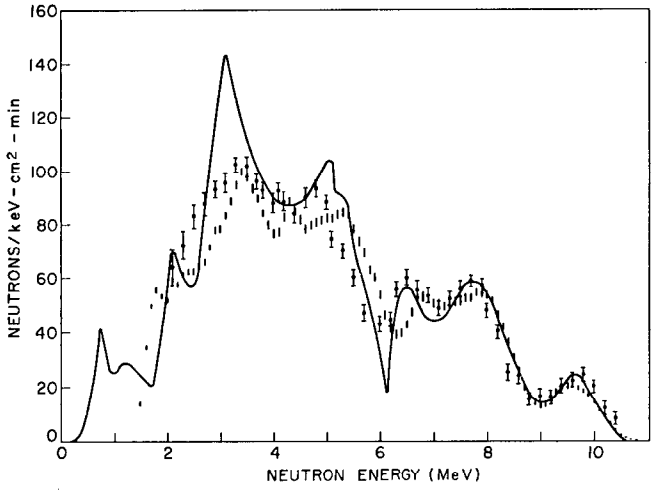

Fig. 4.5—*PuBe* neutron spectra: NRL data (same as Fig. 4.4) shown as the bars indicating the extent of statistical uncertainties, smooth curve is the theoretical calculation by Van der Zwan (13); points with error bars are the data of Rubbino et al. (14). Spectra are normalized to the same value of the integral for data above 6 MeV.

UNCLASSIFIED

The occurrence of peaks in the present measurement at 7.9 and 9.6 MeV is in good agreement with the theoretical predictions, but those at 3.4, 5.4, and 6.7 MeV are somewhat higher than the predicted values. This disagreement may have been introduced by inaccurate γ-ray calibration or an inaccurate value of α in Eq. (2-9) for the electronic system used.

A calibration using neutron moderators and BF_3 detectors at the National Bureau of Standards indicated that 1.38×10^6 neutrons per second were emitted from the *PuBe* source. Integration under the measured spectrum from 2.5 to 10.8 MeV with an adjustment for lower-energy neutrons using Van der Zwan's calculation yields a measured value of 1.3×10^6 neutrons per second, in good agreement with the NBS value.

The energy spectrum of neutrons from an *AmBe* source was also measured, and the derived energy spectrum is presented in Fig. 4.6. The agreement with theory is similar to that for the *PuBe* source. One point to be noted concerning the *AmBe* spectrum is that the dip at 6.1 MeV is shallower than in the *PuBe* spectrum. This is in agreement with the theoretical calculations of Van der Zwan (13).

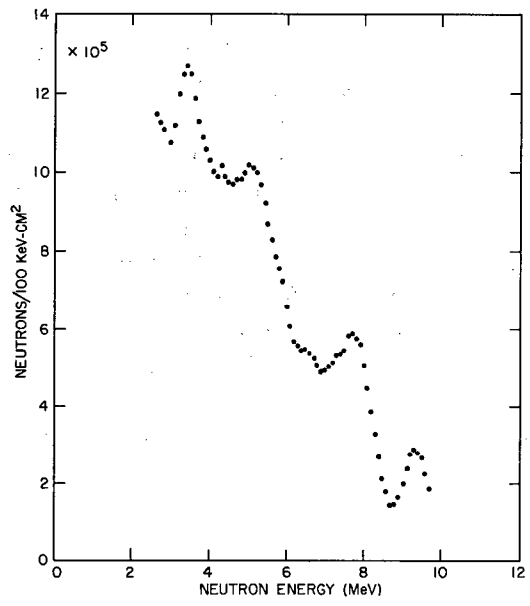

Fig. 4.6—Energy spectrum of neutrons from an *AmBe* source. Since the geometry of exposure was not optimized (as it was for the *PuBe* source, Figs. 4.4 and 4.5), the rise in the spectrum at low energies is due in a large part to scattered neutrons.

4.3. Other Spectra

Besides the measurements just described, this spectrometer has been used to measure two additional spectra: (a) the energy spectrum of neutrons scattered from carbon and (b) the energy spectrum of photoneutrons from the $O^{16}(\gamma,n)O^{15}$ reaction. The energy spectrum of neutrons scattered from C^{12} is shown in Fig. 4.7. For this measurement ring geometry was used with an 18-inch-long brass scattering bar shielding the detector from the 8.0-MeV neutrons produced by a $D(d,n)$ reaction. The scattering ring of carbon was placed such that the scattering angle was 76°, defined by the angle between the line of flight of neutrons incident on the ring and the direction of the detector from the scatterer. In the spectrum, the peak around 6.7 MeV represents neutrons scattered elastically from C^{12}. The peak around 2.7 MeV represents neutrons scattered inelastically from the 4.43-MeV state of C^{12}.